Chapter 3

Energy and exergy analyses of four different combined power and cooling systems integrated with a topping gas turbine plant

In integrated energy systems, the layout of the subsystems must be carefully chosen because even a slight change in the configuration of one subsystem can have a significant impact on the overall performance as described in Chapter 2. The intent to maximize the utilization of the waste heat generated at the power-generating unit is the most crucial factor employed when choosing the configuration of a subsystem or the integration scheme in the bottoming cycle. The appropriate technique for carrying out such a study is to investigate the performance of the integrated system in various configurations. In this regard, the current chapter presents four novel GT-based combined power and cooling (CPC) systems. The CPC systems are configured based on the integration of the simple GT plant with the bottoming cycle that includes the steam turbine (ST) cycle, Recuperative organic Rankine cycle (R-ORC) and absorption cooling systems (ACSs). The topping GT plant is the same in all system configurations and the subsystems of the bottoming cycles are considered with different arrangements. In the first configuration, for driving the R-ORC, extracted steam from the back-pressure type ST is used while in the second configuration; the entire steam from the back-pressure type ST is used as a heat source. Similarly, for the ACS, various heat source options such as the exhaust heat from the heat recovery steam generator (HRSG), steam from back pressure ST and extracted steam from ST are explored. As such, the first and second configu-

rations are GT-ST-ORC-ACS systems while the third and fourth configurations are GT-ST-ACS systems. In the first and fourth configurations, there are two ACSs; one is driven by steam and the other by exhaust gas, while in the second and third configurations, there is only one ACS driven by exhaust gas. To the best of the authors' knowledge, no prior study has previously studied the systems that are being compared in this study.

3.1 Description of CPC system configurations

The layout for the first configuration (system-I) is shown in Fig. 3.1. The topping cycle is a natural gas-fired simple GT plant composed of an air compressor (AC), a combustion chamber (CC), and a GT. The HRSG, which consists of three sections: economizer (ECO), evaporator (EVA), and superheater (SUP), first uses the GT exhaust to produce superheated steam. The steam is then expanded in two stages in the back-pressure steam turbine (ST). Further, after the initial stage of expansion, some steam from the ST is withdrawn to drive the Recuperative ORC (R-ORC). At the end of the second stage, the remaining steam is further withdrawn at a temperature adequate for driving a single effect ACS (ACS-I) that operates on water-LiBr. The heat needed for vapour generation in the corresponding generators of the R-ORC and ACS-I is provided by the two streams of steam. Then, the water streams are pumped to the HRSG after condensation. The exhaust gas at the HRSG exit is further utilized to produce cooling through another water-LiBr operated single effect ACS (ACS-II). The R-ORC consists of the components like the vapour generator (VG), vapour turbine (VT), an internal heat exchanger (IHE), condenser and pump. The VT expands the high-pressure vapour generated in the VG to low pressure to produce work. The IHE preheats the organic liquid by utilizing the heat of low-pressure organic vapour flowing in the reverse direction from the VT outlet. In the condenser, the organic vapour gets condensed to a liquid by rejecting heat to cold water. The cycle is completed by pumping the organic liquid via the IHE back to the VG.

The layout of the second configuration (system-II) is shown in Fig. 3.2. In this system, the superheated steam generated in the HRSG is first expanded in the back-pressure ST then the entire low-pressure steam is directly fed to the VG of the R-ORC for additional power generation. On the other hand, the single-effect ACS is driven by the HRSG exhaust gas for cooling generation. The layout of the third system configuration (system-III) is shown in Fig. 3.3. It is a rather simple system

that consists of the GT plant, the HRSG, and the condensing type ST plant, where there is only one ACS that is driven by the heat from the HRSG exhaust gas. The ST plant consists of one open feedwater heater (OFWH), a condenser and a feed pump. The superheated steam from the HRSG drives the ST. After expansion in the ST, some amount of steam is extracted from the ST for feed water preheating in the OFWH and the remaining steam is expanded up to the condenser pressure. The extracted steam from the ST mixes with the feed water in the OFWH and the mixture in a saturated state is pumped back to the HRSG. The layout of the fourth system configuration (system-IV) is shown in Fig. 3.4. In this system, there are two ACS (ACS-I and ACS-II), with ACS-I being driven by steam extracted from the ST at lower pressure while ACS-II is driven by the heat from the HRSG exhaust gas.

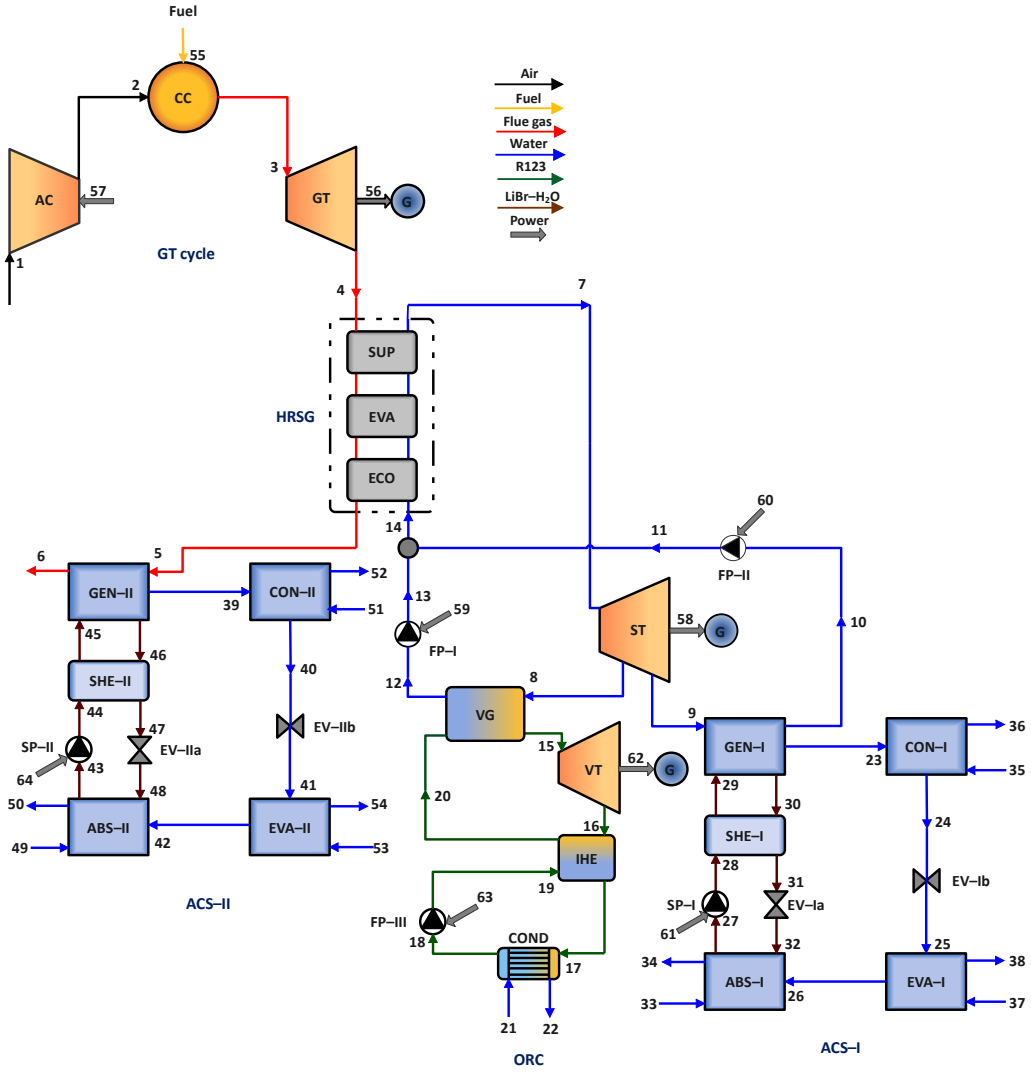

Fig. 3.1: Layout of the first CPC system (CPC system-I).

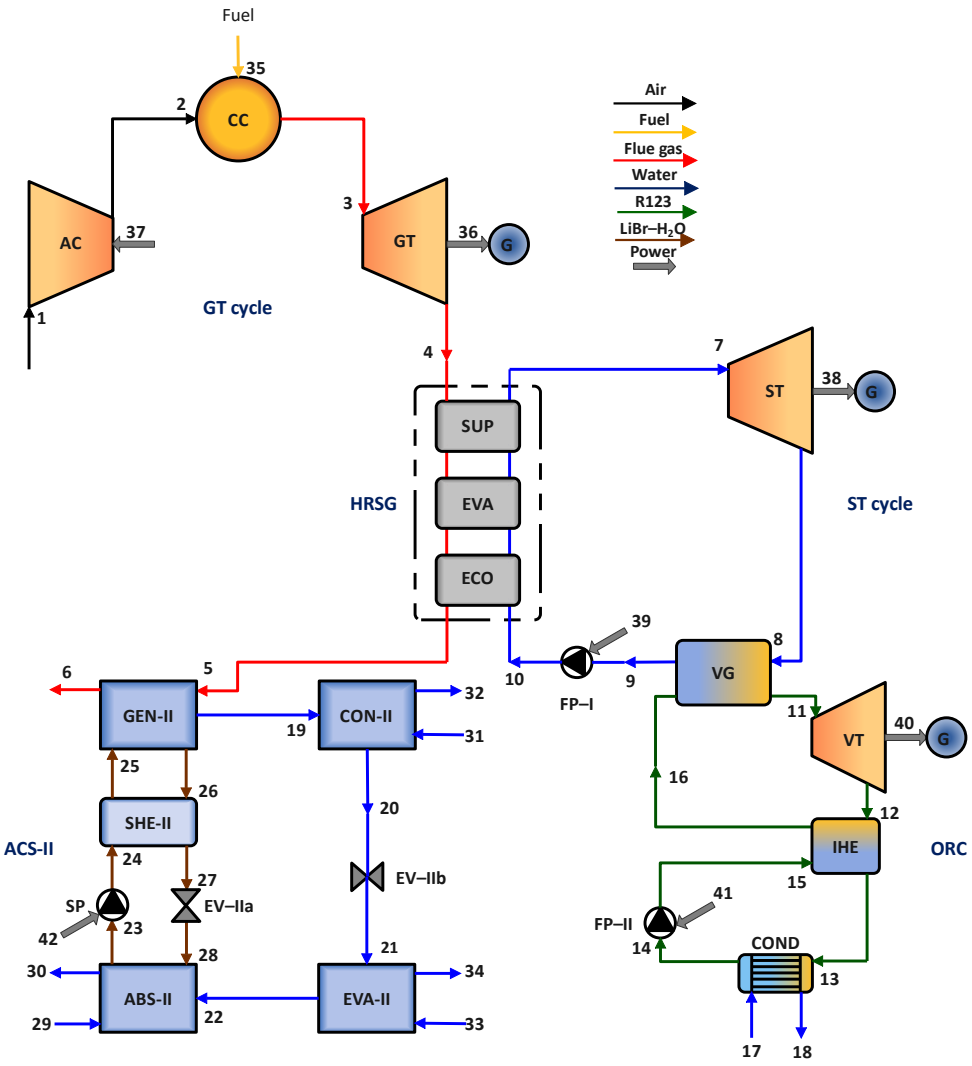

Fig. 3.2: Layout of the second CPC system (CPC system-II).

3.2 Modelling

The assumptions and the input parameters considered for modelling the CPC systems, and the mathematical formulations applied for performing the energy and exergy analyses are discussed in the following subsections.

3.2.1 Assumptions

The assumptions and input parameters considered for modelling the components of the CPC systems are listed below [2, 3, 20]:

- A steady-state condition is assumed for modelling all the components.
- The changes in kinetic and potential energy are neglected.

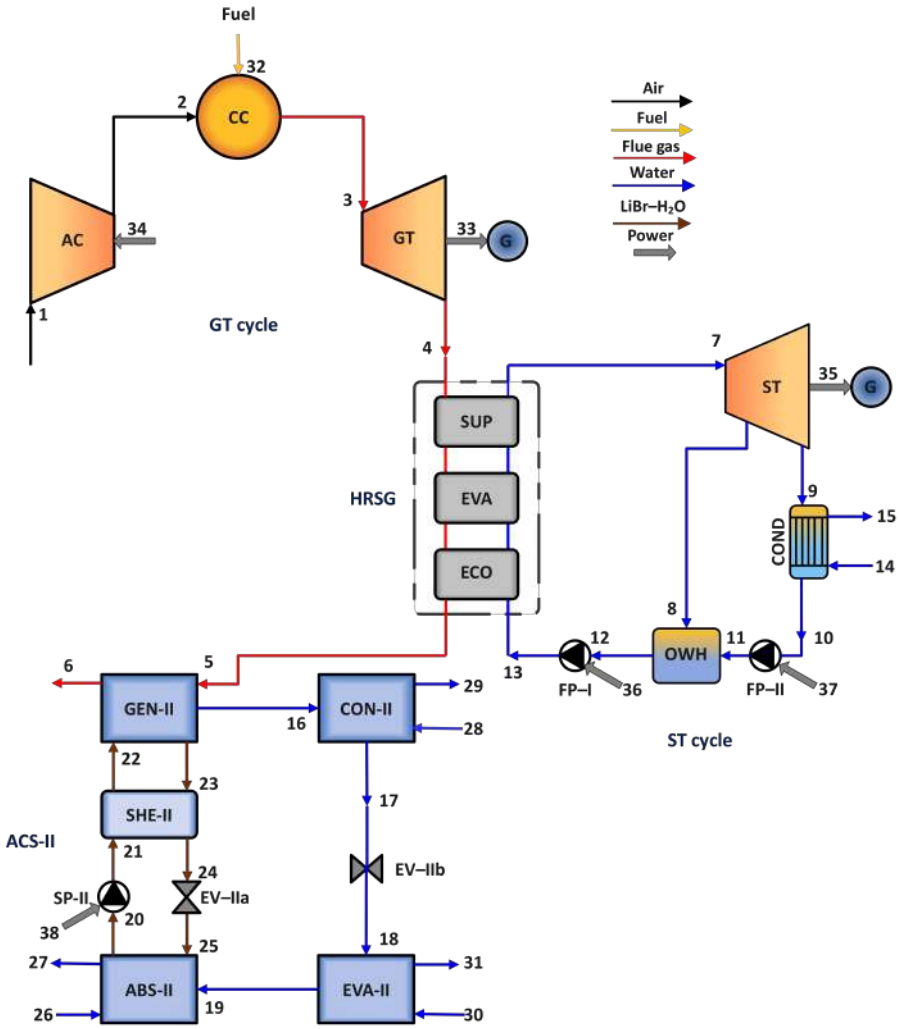

Fig. 3.3: Layout of the third CPC system (CPC system-III).

- The volumetric composition of natural gas is considered as:
  Methane (CH_4) 93.06%, Ethane (C_2H_6) 4.09%, Propane (C_3H_8) 0.99%, Butane (C_4H_{10}) 0.39%, Pentane (C_5H_{12}) 0.16%, Nitrogen (N_2) 0.4%, Carbon dioxide (CO_2) 0.89%.
- Natural gas has a temperature of 333.35 K and a pressure of 2650 kPa.
- The flow rate of air is 80.58 kg/s and heat exchanger's effectiveness is 75%.
- Isentropic efficiency of VT and pumps are 80% and 85%.
- The chemical exergy of the working fluid in the R-ORC is neglected.

The remaining assumed parameters related to the GT cycle, HRSG and ST cycle, and R-ORC and ACS are listed in Tables 3.1 to 3.3, respectively.

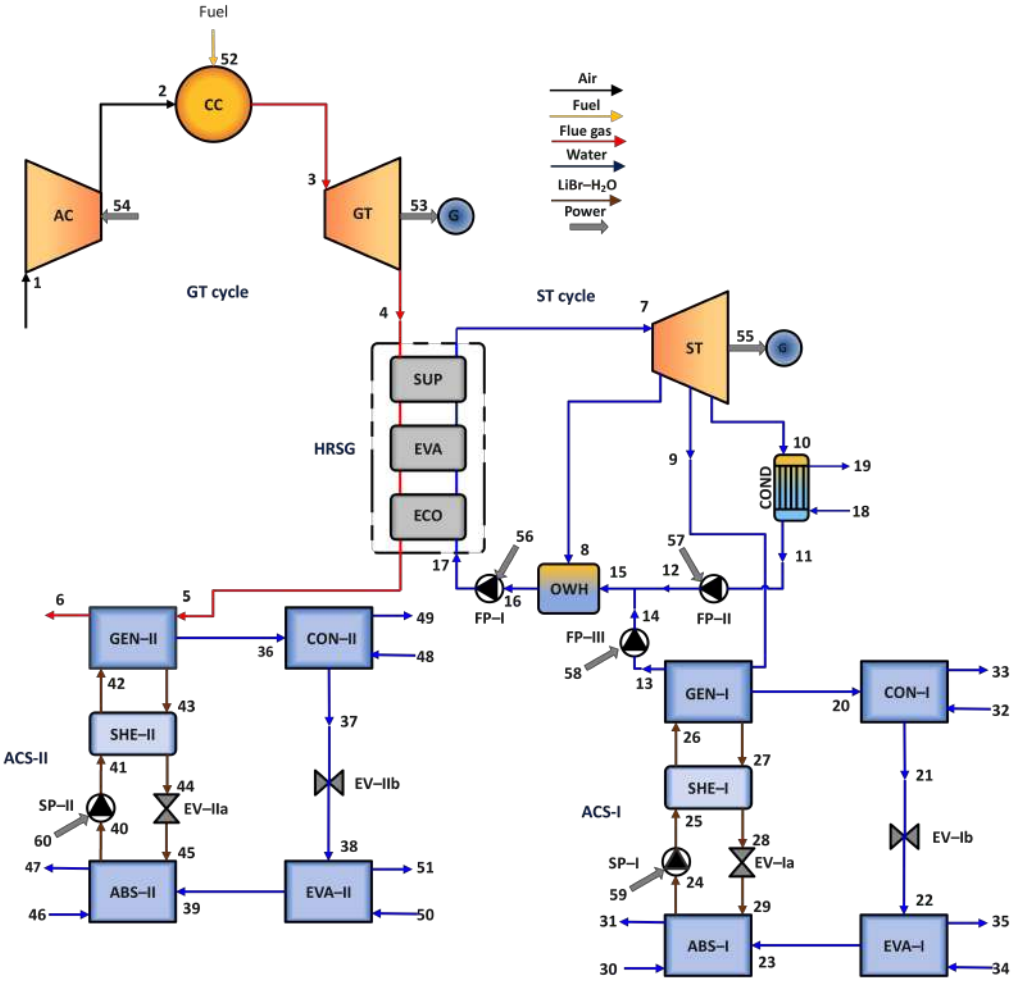

Fig. 3.4: Layout of the forth CPC system (CPC system-IV).

Table 3.1: The input parameters used in the modelling of the GT cycle [10, 14].

Parameters	Symbols	Value	Unit
Fuel flow rate	$\dot{m}_f$	2.68	kg/s
Airflow rate	$\dot{m}_a$	110	kg/s
AC pressure ratio	r_p	10	-
Isentropic efficiency of AC	$\eta_{s,AC}$	86	%
Isentropic efficiency of GT	$\eta_{s,GT}$	86	%
Combustion efficiency	η_{com}	98	%
Generator efficiency	η_{gen}	98	%

3.2.2 Energy analysis

The steady-state mass and energy balance equations for a Control Volume are given by [3]:

$$\sum \dot{m}_i = \sum \dot{m}_e \tag{3.1}$$

Table 3.2: The input parameters used in the modelling of the ST cycle and HRSG [14, 21].

Parameters	Symbols	Value	Unit
ST inlet pressure	P_7	8900	kPa
ST inlet temperature	T_7	823.15	K
ST isentropic efficiency	$\eta_{s,ST}$	90	%
FP isentropic efficiency	$\eta_{s,FP}$	90	%
COND pressure (System-III & -IV)	P_{COND}	5	kPa
OWH pressure (System-III & -IV)	P_{OWH}	500	kPa
HRSG's PPTD	$\Delta T_{pp,HRSG}$	30	K
HRSG's APTD	$\Delta T_{ap,HRSG}$	10	K

Table 3.3: The input parameters used in the modelling of R-ORC and ACS [14, 18].

Parameters	Symbols	Value	Unit
VT inlet temperature (for system-I)	T_{15}	414	K
VT inlet temperature (for system-II)	T_{11}	390	K
COND temperature (for system-I)	T_{17}	303.15	K
COND temperature (for system-II)	T_{13}	303.15	K
Effectiveness of IHE	ω_{IHE}	90	%
Condensate inlet temperature (for system-I)	T_{21}	298.15	K
Condensate outlet temperature (for system-I)	T_{22}	303.15	K
Condensate inlet temperature (for system-II)	T_{17}	298.15	K
Condensate outlet temperature (for system-II)	T_{18}	303.15	K
VT isentropic efficiency	$\eta_{s,VT}$	90	%
VG's PPTD	$\Delta T_{pp,VG}$	10	K
ABS-I/II inlet water temperature	$T_{ABS-I/II,in}$	298.15	K
ABS-I/II outlet water temperature	$T_{ABS-I/II,out}$	303.15	K
EVA-I/II inlet water temperature	$T_{EVA-I/II,in}$	288.15	K
EVA-I/II outlet water temperature	$T_{EVA-I/II,out}$	283.15	K
CON-I/II inlet water temperature	$T_{CON-I/II,in}$	298.15	K
CON-I/II outlet water temperature	$T_{CON-I/II,out}$	303.15	K
GEN-I/II temperature	$T_{GEN-I/II}$	363.15	K
ABS-I/II temperature	$T_{ABS-I/II}$	308.15	K
CON-I/II temperature	$T_{CON-I/II}$	308.15	K
EVA-I/II temperature	$T_{EVA-I/II}$	278.15	K
SP-I/II isentropic efficiency	$\eta_{s,SP-I/II}$	90	%
SHE-I/II effectiveness	$\omega_{SHE-I/II}$	75	%

$$\sum(\dot{m}h)_i + \sum\dot{Q} = \sum(\dot{m}h)_e + \sum\dot{W} \tag{3.2}$$

Eq. (3.1) and Eq. (3.2) are applied considering that each component of the proposed CPC systems is enclosed within the imaginary control volume. Besides, the governing equations developed for modelling the components of CPC systems are

described in the following subsections:

GT cycle modelling

The volumetric composition of ambient air for the given ambient condition (60%, 298.15 K, 101.3 kPa) is estimated to be [19]:
N_2: 76.63%, O_2: 20.56%, Ar: 0.92%, CO_2: 0.03%, H_2O:1.86%.

Then based on the evaluated air composition, the specific enthalpy (h_1) and entropy (s_1) are calculated at the inlet of AC using REFPROP 9.0 [13]. REFPROP is a computer programme that offers thermophysical parameters of pure fluids and mixtures throughout a wide variety of fluid states, including liquid, gas, and supercritical phases. To specify the state, the REFPROP routine needs the value of two thermophysical parameters, and once the state is determined, it provides a third unidentified thermophysical parameter. It is developed by the Standard Reference Data programme of the National Institute of Standards and Technology (NIST). The next step is to calculate the pressure at the outlet of the AC using Eq. (3.3) [3].

$$P_2 = P_1 \times r_p \tag{3.3}$$

where r_p is the AC pressure ratio.

Then, taking into consideration the isentropic compression, the specific entropy in the isentropic state at the AC outlet (s_{2s}) is set equal to that of AC intake (s_1). The REFPROP routine is then used to determine the temperature at the isentropic state at the AC outlet (T_{2s}) using the inputs P_2 and s_{2s}. Similar to this, the REFPROP routine is used to estimate the specific enthalpy at the isentropic state at the AC outlet (h_{2s}) by passing P_2 and T_{2s} as input. The specific enthalpy at the actual state of the AC outlet is then computed using Eq. (3.4) [3].

$$h_2 = h_1 + \frac{h_{2,s} - h_1}{\eta_{s,AC}} \tag{3.4}$$

Then, by providing P_2 and h_2 as input to the REFPROP routine, the specific entropy (s_2) and temperature (T_2) at the AC outlet are computed. The work consumed at the AC is then calculated using Eq. (3.5) [2].

$$\dot{W}_{AC} = \dot{m}_a(h_2 - h_1) \tag{3.5}$$

where $\dot{m}_a$ is the mass flow rate of air.

Then the CC is modelled by solving the combustion reaction considering the

known air flow rate and fuel flow rate. The stoichiometric and actual molar air-fuel ratio is found to be 2.092 and 5.204, respectively, with an excess air of 147.7%. The combustion reaction for 1 kmol of natural gas is given as follows [20]:

$$0.9306\,CH_4 + 0.0411\,C_2H_6 + 0.0099\,C_3H_8 + 0.0039\,C_4H_{10} + 0.0016\,C_5H_{12} + 0.0089\,CO_2 + 0.004\,N_2 + 2.101\,[2.477\,(O_2 + 3.7271\,N_2 + 0.0015\,CO_2 + 0.0905\,H_2O + 0.0447\,Ar)] \longrightarrow 19.325\,N_2 + 3.302\,O_2 + 1.0827\,CO_2 + 2.10\,H_2O + 0.231\,Ar \quad (3.6)$$

The lower heating value ($\overline{LHV}$) of fuel in kJ/kmol is calculated by using Eq. (3.7) [20].

$$\overline{LHV} = -\left[\sum_P \dot{n}_P \bar{h}^0_{d,P} - \sum_R \dot{n}_R \bar{h}^0_{d,R}\right] \quad (3.7)$$

In Eq. (3.7), $\dot{n}$ corresponds to the molar coefficients of products (P) and reactants (R) and $\bar{h}^0_d$ is the standard molar specific enthalpy of devaluation [12].

The volumetric composition of the combustion gas leaving the CC is estimated using the combustion equation. Then using the energy balance equation shown in Eq. (3.8) [9], the specific enthalpy at the outlet of CC is determined.

$$h_3 = \frac{\dot{m}_a h_2 + \dot{m}_f LHV \eta_{comb}}{\dot{m}_g} \quad (3.8)$$

where $\dot{m}_f$ and $\dot{m}_g$ are the mass flow rate of air and combustion gas, respectively.

The pressure (P_3) of the combustion gas exiting the CC is calculated using a pressure drop of 1.5% [3]. Next, h_3 and P_3 are passed as input to the REFPROP routine to compute the temperature (T_3) and specific entropy (s_3) of the combustion gas at the CC outlet.

The pressure (P_4) of the combustion gas exiting the GT is calculated using a pressure drop of 3% [3]. The specific entropy in the isentropic state at the GT outlet (s_{4s}) is then set equal to that of the GT inlet (s_3), taking into account the isentropic expansion. The REFPROP routine is then used to determine the temperature (T_{4s}) and specific enthalpy (h_{4s}) at the isentropic state at the GT outlet using the inputs P_4 and s_{4s}. The specific enthalpy at the actual state at the GT outlet is then computed using Eq. (3.9) [3].

$$h_4 = h_3 - \eta_{s,GT}(h_3 - h_{4s}) \quad (3.9)$$

Then, by providing P_4 and h_4 as input to the REFPROP routine, the specific entropy (s_4) and temperature (T_4) at the GT outlet are computed. The work produced by the GT is calculated using Eq. (3.10) and the net work obtained from the topping

GT cycle is calculated using Eq. (3.11) [3].

$$\dot{W}_{GT} = \dot{m}_g(h_3 - h_4) \tag{3.10}$$

$$\dot{W}_{net,GT} = \eta_{gen}(\dot{W}_{GT} - \dot{W}_{AC}) \tag{3.11}$$

HRSG and ST modelling

The HRSG is designed in a single-pressure mode. The PPTD of 30 K is considered for modelling the HRSG. It implies that there is a difference of 30 K between the saturation temperature of water at a given pressure and the temperature of the combustion gas leaving the evaporator. Besides, the specific enthalpy and entropy of water at the inlet and outlet of the HRSG were calculated using REFPROP 9.0 [13]. In addition, the unknown temperature of the steam and flue gases at the entry and exit of each segment of the HRSG is determined using the heat balance for each segment separately. The amount of heat recovered at the HRSG is evaluated using Eq. (3.12) [9].

$$\dot{Q}_{HRSG} = \dot{m}_g(h_4 - h_5) \tag{3.12}$$

The correlation used for determining the steam generation rates obtained from the HRSGs corresponding to system-I, system-II,system-III and system-IV are shown in Eq. (3.13) [3].

$$\dot{m}_s = \dot{m}_g \left(\frac{h_4 - h_{4p}}{h_7 - h_{7s}} \right) \tag{3.13}$$

where $\dot{m}_s$ is the steam generation rate, h_{4p} is the specific enthalpy corresponding to the flue gas at the exit of the economizer and h_{7s} is the specific enthalpy of water at the saturation temperature.

The ST is modelled considering isentropic expansion, while the pumps are modelled considering isentropic compression. Meanwhile, the steady flow energy equation is used to calculate the work produced by the ST as well as the work consumed by the pumps. The net ST power is determined using Eq. (3.14) [9].

$$\dot{W}_{net,ST} = \dot{W}_{ST} \times \eta_{gen} - \dot{W}_{pump/pumps} \tag{3.14}$$

R-ORC modelling

R123 is chosen as the working medium for operating the R-ORC employed in system-I and system-II. The thermodynamic properties of R123 at various states of the R-ORC are determined using REFPROP 9.0 [13]. R123 is preferred over other organic

fluids because of its low global warming potential, low ozone depletion potential, and short atmospheric life [23]. Additionally, R123 has been deemed the best organic fluid for R-ORC operation in waste heat recovery applications in numerous fluid selection studies [1, 7, 24]. Further, a PPTD of 10 K is used to model the heat transfer between R123 and the flue gas in the VG of the R-ORCs [2]. The condition of R123 at the VT inlet and COND outlet are considered as saturated vapour and saturated liquid, respectively. The net power ($\dot{W}_{net}$) obtained from the R-ORCs is calculated as follows [11].

$$\dot{W}_{net,R-ORC} = \dot{W}_{VT} - \sum \dot{W}_{Pump} \tag{3.15}$$

where $\dot{W}_{VT}$ is the power produced by the VT and $\dot{W}_{Pump}$ is the work consumed by the pump.

The energy efficiency of the R-ORC can be determined using Eq. (3.16) [11].

$$\eta_{R-ORC} = \frac{\dot{W}_{net,R-ORC}}{\dot{Q}_{VG}} \tag{3.16}$$

where $\dot{Q}_{VG}$ is the heat recovered from the flue gas in the VG.

ACS modelling

The mass percentage (X) of LiBr in a strong solution (ss) and weak solution (ws) are evaluated using the equations given below [18]:

$$X_{ss} = \frac{49.04 + 1.125T_{GEN} - T_{CON}}{134.65 + 0.47T_{GEN}} \tag{3.17}$$

$$X_{ws} = \frac{49.04 + 1.125T_{ABS} - T_{EVA}}{134.65 + 0.47T_{ABS}} \tag{3.18}$$

where T_{GEN},T_{ABS},T_{EVA} and T_{CON} are the operating temperatures of generator, absorber, evaporator and condenser, respectively, in °C.

The pressure level at which the evaporator and condenser operate are determined using Eq. (3.19) [18].

$$P = 10^5 exp\left(\frac{11.78(T - 372.79)}{T - 43.15}\right) \tag{3.19}$$

where T is the operating temperature of the condenser or evaporator in Kelvin.

As a matter of fact, once the operating pressures of the condenser and evaporator are established, the pressure level of the entire ACS setup is also known because

the operating pressures of the generator and absorber are identical to those of the condenser and evaporator, respectively. Besides, the thermodynamic properties of the LiBr-H_2O solution are calculated using the explicit functions of Patek and Klomfar [16] while REFPROP 9.0 [13] is used for determining the properties of H_2O at vapour and liquid states. The heat source for the ACS-I's generator is the exhaust gas leaving the HRSG, which rejects the heat and leaves the generator at 100 °C. Similarly, for the ACS-II's generator, the condensing steam at 100 °C is the heat source for vapour generation. As such, the heat supplied to the generator of the ACS ($\dot{Q}_{GEN,S}$) is known beforehand. Alternately, for the ACS, the generator heat load ($\dot{Q}_{GEN,R}$) can be expressed in terms of enthalpy and flow rates. For instance, the heat load of ACS–I's generator in system-I is given by [14]:

$$\dot{Q}_{GEN,R,ACS-I} = \dot{m}_{\mathrm{H_2O}} h_{39} - \dot{m}_{ss} h_{46} - \dot{m}_{ws} h_{45} \tag{3.20}$$

Similarly, the same method can be used to determine the heat load for the ACS-II generator. The evaporator cooling load ($\dot{Q}_{EVA}$) is first assumed. The flow rate of H_2O, strong solutions and weak solutions are then determined by iterating the $\dot{Q}_E$ until $\dot{Q}_{GEN,R}$ becomes equal to $\dot{Q}_{GEN,S}$. Thus ($\dot{Q}_{EVA}$) is an output of the present analysis. The logical sequence used in modelling the ACS-I of system-I is shown in Fig. 3.5. Then the COPs of the ACS-I and ACS-II in each of the four CPC systems are evaluated using the correlation presented in Eq. (3.21) [18]. The mass flow rates of water flowing through the external circuits of the evaporator, absorber and condenser are determined by solving the respective heat balance equations.

$$COP = \frac{\dot{Q}_{EVA}}{\dot{Q}_{GEN} + \dot{W}_{SP}} \tag{3.21}$$

3.2.3 Exergy analysis

Exergy in a specific state can be broadly divided into four components: physical, chemical, potential, and kinetic exergy, as shown in Eq. (3.22) [3].

$$\dot{E} = \dot{E}_{ph} + \dot{E}_{ch} + \dot{E}_{pt} + \dot{E}_{kt} \tag{3.22}$$

where $\dot{E}_{ph}$, $\dot{E}_{ch}$, $\dot{E}_{pt}$, and $\dot{E}_{kt}$ are the rates of physical, chemical, potential, and kinetic exergy, respectively.

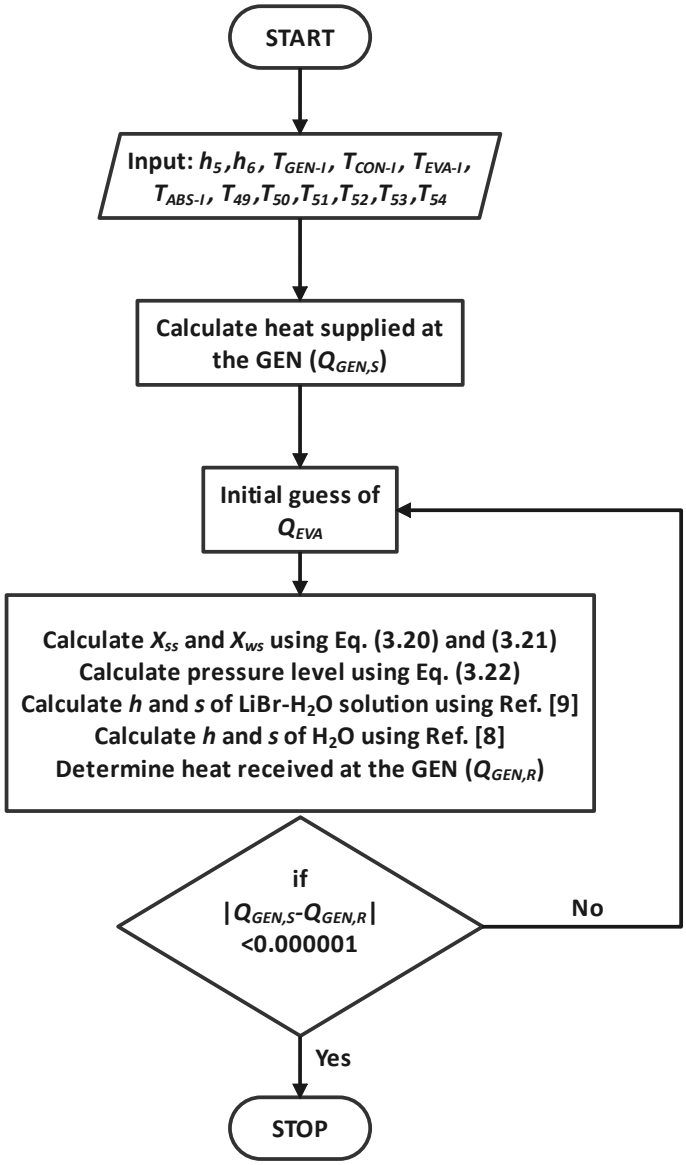

Fig. 3.5: A flowchart describing the ACS modelling procedure.

The physical exergy is the maximum theoretically useful work that can be produced as a system progresses from its initial state with temperature and pressure of T and P to the dead state with temperature and pressure of T_0 and P_0. The correlation used for evaluating the physical exergy is shown in Eq. (3.23) [3]. Furthermore, due to the assumption of steady state, both potential and kinetic exergy are assumed to be zero.

$$\dot{E}_{ph} = \dot{m}[(h - h_0) - T_0(s - s_0)] \tag{3.23}$$

On the other hand, the chemical exergy is the maximum theoretically useful work as the system progresses from the limited dead state to the dead state where it is

completely in equilibrium with the environment [3]. The chemical exergy of flue gas ($\dot{E}_{fg}^{CH}$) is calculated using Eq. (3.24) [3].

$$\dot{E}_{fg}^{CH} = \dot{n}_{fg} \sum_{k} x_k [\bar{e}_k^{CH} + \bar{R} T_0 ln(x_k)] \tag{3.24}$$

where $\dot{n}_{fg}$ is the molar flow rate of the flue gas, x_k is the mole fraction of the flue gas component k, $\bar{R}$ is the universal gas constant and $\bar{e}_k^{CH}$ is the chemical exergy per mole of component k [3].

The chemical exergy of air is calculated by using Eq. (3.25) [3]:

$$\dot{E}_{a}^{CH} = \dot{n}_{a} \sum_{k} x_k \bar{e}_k^{CH} \tag{3.25}$$

where $\dot{n}_a$ is the molar flow rate of air, x_k is the mole fraction of the gaseous component k present in the air.

The chemical exergy of the working medium in the R-ORC is ignored, whereas that of water is computed by using Eq. (3.26) [3]:

$$\dot{E}_{\mathrm{H_2O}}^{CH} = \frac{\dot{m}}{M_{\mathrm{H_2O}}} \left(\bar{e}_{\mathrm{H_2O}}^{CH} \right) \tag{3.26}$$

The chemical exergy of LiBr-H_2O solution in the ACSs is calculated using the following expression [15].

$$\dot{E}_{LiBr-\mathrm{H_2O}}^{CH} = \frac{\dot{m}}{M_{sol}} \left[\sum_{k} x_k \bar{e}_k^{CH} + \bar{R} T_0 \sum_{k} x_k ln(a_k) \right] \tag{3.27}$$

where a_k is the activity of species k, defined as the ratio of the vapour pressure of species k in the mixture to the vapour pressure of pure species. M_{sol} is the molecular weight of the LiBr-H_2O solution. The activity of LiBr and H_2O is calculated using the method given in Ref. [15].

The exergy balance equation is given by [3]:

$$\dot{E}_F = \dot{E}_P + \dot{E}_D + \dot{E}_L \tag{3.28}$$

where $\dot{E}_F$, $\dot{E}_P$, $\dot{E}_D$ and $\dot{E}_L$ denote the rate of fuel exergy, product exergy, exergy destroyed and the exergy loss, respectively.

The product exergy is the desired output of a system, while the fuel exergy is the exergy used to achieve that output. Exergy loss denotes the exergy that leaves the system without being utilized, while exergy destruction is the loss in exergy

due to the irreversibility of the system. The exergy balance equations for all the components of the four configurations of CPC systems are shown in Tables 3.4 to 3.5, respectively. In exergy analysis, exergy efficiency and exergy destruction ratio are very useful performance criteria for assessing the individual performance of the subsystem components. Exergy efficiency is defined as the ratio of the product exergy to the fuel exergy. It measures the true performance of a system component and helps in identifying components requiring attention. The generalized expression for exergy efficiency (ε) is given in Eq. (3.29) [3]. On the other hand, the exergy destruction ratio (Y_D) is defined as the ratio of exergy destruction in a component to the overall exergy destruction of the system. The expression for exergy destruction ratio is given in Eq. (3.30) [3].

$$\varepsilon = \frac{\dot{E}_P}{\dot{E}_F} \tag{3.29}$$

$$Y_D = \frac{\dot{E}_{D,k}}{\dot{E}_{D,overall}} \tag{3.30}$$

3.2.4 Overall performance criteria

The parameters considered for evaluating the overall performance of four CPC systems are defined as follows:

Energy efficiency

The energy efficiency of the topping GT cycle is given by [5]:

$$\eta_{GTcycle} = \frac{\dot{W}_{net,GT}}{\dot{m}_f LHV} \tag{3.31}$$

Similarly, the energy efficiency of the ST cycle and R-ORC are given by Eq. (3.32) and Eq. (3.33), respectively [14]:

$$\eta_{STcycle} = \frac{\dot{W}_{net,ST}}{\dot{Q}_{HRSG}} \tag{3.32}$$

$$\eta_{R-ORC} = \frac{\dot{W}_{net,R-ORC}}{\dot{Q}_{VG}} \tag{3.33}$$

where $\dot{Q}_{HRSG}$ and $\dot{Q}_{VG}$ are the heat recovered from the HRSG and VG, respectively.

The overall energy efficiency of the CPC systems is given by [5]:

$$\eta_{tot} = \frac{\dot{W}_{net,GT} + \dot{W}_{net,ST} + \dot{W}_{net,R-ORC} + \sum \dot{Q}_{cooling}}{\dot{m}_f LHV} \tag{3.34}$$

where $\dot{Q}_{cooling}$ is the cooling load obtained from the ACS.

Exergy efficiency

The exergy efficiency of the topping GT cycle is given by [5]:

$$\varepsilon_{GTcycle} = \frac{\dot{W}_{net,GT}}{\dot{E}_1 + \dot{E}_f} \tag{3.35}$$

where $\dot{E}_f$ is the exergy of fuel fed to the CC.

Likewise, the exergy efficiency of the ST cycle is given by Eq. (3.36) [14].

$$\varepsilon_{STcycle} = \frac{\dot{W}_{net,ST}}{(\dot{E}_4 - \dot{E}_5)} \tag{3.36}$$

The exergy efficiency of the R-ORC in system-I and system-II are shown in Eq. (3.37) and Eq. (3.38), respectively [14]:

$$\varepsilon_{R-ORC/system-I} = \frac{\dot{W}_{net,R-ORC}}{(\dot{E}_8 - \dot{E}_{12})} \tag{3.37}$$

$$\varepsilon_{R-ORC/system-II} = \frac{\dot{W}_{net,R-ORC}}{(\dot{E}_8 - \dot{E}_9)} \tag{3.38}$$

The overall exergy efficiency of the CPC systems is given by [5]:

$$\varepsilon_{tot} = \frac{\dot{W}_{net,GT} + \dot{W}_{net,ST} + \dot{W}_{net,R-ORC} + \sum \Delta \dot{E}_{EVA}}{\dot{E}_1 + \dot{E}_f} \tag{3.39}$$

where $\Delta \dot{E}_{EVA}$ is the exergy change at the evaporator of the ACSs.

3.3 Results and discussion

3.3.1 Model validation

The proposed CPC systems are simulated using an in-house built code based on a MATLAB environment. The code's accuracy is verified by comparing the results to

Table 3.4: Exergy balance equations for all components of system-I and system-II.

Components	System-I	System-II
AC	$\dot{E}_{57} = \dot{E}_2 - \dot{E}_1 + \dot{E}_D$	$\dot{E}_{37} = \dot{E}_2 - \dot{E}_1 + \dot{E}_D$
CC	$\dot{E}_2 + \dot{E}_{55} = \dot{E}_3 + \dot{E}_D$	$\dot{E}_2 + \dot{E}_{35} = \dot{E}_3 + \dot{E}_D$
GT	$\dot{E}_3 - \dot{E}_4 = \dot{E}_{56} + \dot{E}_{57} + \dot{E}_D$	$\dot{E}_3 - \dot{E}_4 = \dot{E}_{36} + \dot{E}_{37} + \dot{E}_D$
HRSG	$\dot{E}_4 - \dot{E}_5 = \dot{E}_7 - \dot{E}_{14} + \dot{E}_D$	$\dot{E}_4 - \dot{E}_5 = \dot{E}_7 - \dot{E}_{10} + \dot{E}_D$
ST	$\dot{E}_7 - \dot{E}_8 - \dot{E}_9 = \dot{E}_{58} + \dot{E}_{59} + \dot{E}_{60} + \dot{E}_D$	$\dot{E}_7 - \dot{E}_8 = \dot{E}_{38} + \dot{E}_{39} + \dot{E}_D$
VG	$\dot{E}_8 - \dot{E}_{12} = \dot{E}_{15} - \dot{E}_{20} + \dot{E}_D$	$\dot{E}_8 - \dot{E}_9 = \dot{E}_{11} - \dot{E}_{16} + \dot{E}_D$
VT	$\dot{E}_{15} - \dot{E}_{16} = \dot{E}_{61} + \dot{E}_{62} + \dot{E}_{64} + \dot{E}_D$	$\dot{E}_{11} - \dot{E}_{12} = \dot{E}_{40} + \dot{E}_{41} + \dot{E}_{42} + \dot{E}_D$
IHE	$\dot{E}_{16} - \dot{E}_{17} = \dot{E}_{20} - \dot{E}_{19} + \dot{E}_D$	$\dot{E}_{12} - \dot{E}_{13} = \dot{E}_{16} - \dot{E}_{15} + \dot{E}_D$
COND	$\dot{E}_{17} - \dot{E}_{18} = \dot{E}_{22} - \dot{E}_{21} + \dot{E}_D$	$\dot{E}_{13} - \dot{E}_{14} = \dot{E}_{18} - \dot{E}_{17} + \dot{E}_D$
FP-I	$\dot{E}_{59} = \dot{E}_{13} - \dot{E}_{12} + \dot{E}_D$	$\dot{E}_{39} = \dot{E}_{10} - \dot{E}_9 + \dot{E}_D$
FP-II	$\dot{E}_{60} = \dot{E}_{11} - \dot{E}_{10} + \dot{E}_D$	$\dot{E}_{41} = \dot{E}_{15} - \dot{E}_{14} + \dot{E}_D$
FP-III	$\dot{E}_{63} = \dot{E}_{19} - \dot{E}_{18} + \dot{E}_D$	-
GEN-I	$\dot{E}_9 - \dot{E}_{10} = \dot{E}_{23} + \dot{E}_{30} - \dot{E}_{29} + \dot{E}_D$	-
ABS-I	$\dot{E}_{26} + \dot{E}_{32} - \dot{E}_{27} = \dot{E}_{34} - \dot{E}_{33} + \dot{E}_D$	-
CON-I	$\dot{E}_{23} - \dot{E}_{24} = \dot{E}_{36} - \dot{E}_{35} + \dot{E}_D$	-
EVA-I	$\dot{E}_{25} - \dot{E}_{26} = \dot{E}_{38} - \dot{E}_{37} + \dot{E}_D$	-
SHE-I	$\dot{E}_{30} - \dot{E}_{31} = \dot{E}_{29} - \dot{E}_{28} + \dot{E}_D$	-
SP-I	$\dot{E}_{61} = \dot{E}_{28} - \dot{E}_{27} + \dot{E}_D$	-
GEN-II	$\dot{E}_5 - \dot{E}_6 = \dot{E}_{39} + \dot{E}_{46} - \dot{E}_{45} + \dot{E}_D$	$\dot{E}_5 - \dot{E}_6 = \dot{E}_{19} + \dot{E}_{26} - \dot{E}_{25} + \dot{E}_D$
ABS-II	$\dot{E}_{42} + \dot{E}_{48} - \dot{E}_{43} = \dot{E}_{50} - \dot{E}_{49} + \dot{E}_D$	$\dot{E}_{22} + \dot{E}_{28} - \dot{E}_{23} = \dot{E}_{30} - \dot{E}_{29} + \dot{E}_D$
CON-II	$\dot{E}_{39} - \dot{E}_{40} = \dot{E}_{52} - \dot{E}_{51} + \dot{E}_D$	$\dot{E}_{19} - \dot{E}_{20} = \dot{E}_{32} - \dot{E}_{31} + \dot{E}_D$
EVA-II	$\dot{E}_{41} - \dot{E}_{42} = \dot{E}_{54} - \dot{E}_{53} + \dot{E}_D$	$\dot{E}_{21} - \dot{E}_{22} = \dot{E}_{34} - \dot{E}_{33} + \dot{E}_D$
SHE-II	$\dot{E}_{46} - \dot{E}_{47} = \dot{E}_{45} - \dot{E}_{44} + \dot{E}_D$	$\dot{E}_{26} - \dot{E}_{27} = \dot{E}_{25} - \dot{E}_{24} + \dot{E}_D$
SP-II	$\dot{E}_{64} = \dot{E}_{44} - \dot{E}_{43} + \dot{E}_D$	$\dot{E}_{42} = \dot{E}_{24} - \dot{E}_{23} + \dot{E}_D$

data published in the literature. Since the proposed systems are novel, there are no comparable system configurations to validate. As a result, the overall system model is validated by comparing the results of the subsystems to the existing literature separately. The validation of the GT-HRSG integrated model, R-ORC model, ACS model, and ST cycle model are presented in the following subsections.

GT-HRSG system

The integrated GT-HRSG model is validated by comparing the results with the identical model reported in Ref. [3]. Table 3.6 shows a comparison of thermodynamic properties for each state point in both models. Furthermore, Table 3.6 compares several important performance parameters obtained from both models along with the associated deviation. With a maximum deviation of 2.8%, it can be seen that the results from the present GT-HRSG model and those from Ref. [3] exhibit good agreement.

Table 3.5: Exergy balance equations for all components of system-III and system-IV.

Components	System-III	System-IV
AC	$\dot{E}_{34} = \dot{E}_2 - \dot{E}_1 + \dot{E}_D$	$\dot{E}_{54} = \dot{E}_2 - \dot{E}_1 + \dot{E}_D$
CC	$\dot{E}_2 + \dot{E}_{32} = \dot{E}_3 + \dot{E}_D$	$\dot{E}_2 + \dot{E}_{52} = \dot{E}_3 + \dot{E}_D$
GT	$\dot{E}_3 - \dot{E}_4 = \dot{E}_{33} + \dot{E}_{34} + \dot{E}_D$	$\dot{E}_3 - \dot{E}_4 = \dot{E}_{53} + \dot{E}_{54} + \dot{E}_D$
HRSG	$\dot{E}_4 - \dot{E}_5 = \dot{E}_7 - \dot{E}_{13} + \dot{E}_D$	$\dot{E}_4 - \dot{E}_5 = \dot{E}_7 - \dot{E}_{17} + \dot{E}_D$
ST	$\dot{E}_7 - \dot{E}_8 - \dot{E}_9 = \dot{E}_{35} + \dot{E}_{36} +$ $\dot{E}_{37} + \dot{E}_{38} + \dot{E}_D$	$\dot{E}_7 - \dot{E}_8 - \dot{E}_9 - \dot{E}_{10} = \dot{E}_{55} + \dot{E}_{56} +$ $\dot{E}_{57} + \dot{E}_{58} + \dot{E}_{59} + \dot{E}_{60} + \dot{E}_D$
COND	$\dot{E}_9 - \dot{E}_{10} = \dot{E}_{29} - \dot{E}_{28} + \dot{E}_D$	$\dot{E}_{10} - \dot{E}_{11} = \dot{E}_{19} - \dot{E}_{18} + \dot{E}_D$
OWH	$\dot{E}_8 + \dot{E}_{11} = \dot{E}_{12} + \dot{E}_D$	$\dot{E}_8 + \dot{E}_{15} = \dot{E}_{16} + \dot{E}_D$
FP-I	$\dot{E}_{36} = \dot{E}_{13} - \dot{E}_{12} + \dot{E}_D$	$\dot{E}_{56} = \dot{E}_{17} - \dot{E}_{16} + \dot{E}_D$
FP-II	$\dot{E}_{37} = \dot{E}_{11} - \dot{E}_{10} + \dot{E}_D$	$\dot{E}_{57} = \dot{E}_{12} - \dot{E}_{11} + \dot{E}_D$
FP-III	-	$\dot{E}_{58} = \dot{E}_{14} - \dot{E}_{13} + \dot{E}_D$
GEN-I	-	$\dot{E}_9 - \dot{E}_{13} = \dot{E}_{20} + \dot{E}_{27} - \dot{E}_{26} + \dot{E}_D$
ABS-I	-	$\dot{E}_{23} + \dot{E}_{29} - \dot{E}_{24} = \dot{E}_{31} - \dot{E}_{30} + \dot{E}_D$
CON-I	-	$\dot{E}_{20} - \dot{E}_{21} = \dot{E}_{33} - \dot{E}_{32} + \dot{E}_D$
EVA-I	-	$\dot{E}_{22} - \dot{E}_{23} = \dot{E}_{35} - \dot{E}_{34} + \dot{E}_D$
SHE-I	-	$\dot{E}_{27} - \dot{E}_{28} = \dot{E}_{26} - \dot{E}_{25} + \dot{E}_D$
SP-I	-	$\dot{E}_{59} = \dot{E}_{25} - \dot{E}_{24} + \dot{E}_D$
GEN-II	$\dot{E}_5 - \dot{E}_6 = \dot{E}_{16} + \dot{E}_{23} - \dot{E}_{22} + \dot{E}_D$	$\dot{E}_5 - \dot{E}_6 = \dot{E}_{36} + \dot{E}_{43} - \dot{E}_{42} + \dot{E}_D$
ABS-II	$\dot{E}_{19} + \dot{E}_{25} - \dot{E}_{20} = \dot{E}_{27} - \dot{E}_{26} + \dot{E}_D$	$\dot{E}_{39} + \dot{E}_{45} - \dot{E}_{40} = \dot{E}_{47} - \dot{E}_{46} + \dot{E}_D$
CON-II	$\dot{E}_{16} - \dot{E}_{17} = \dot{E}_{29} - \dot{E}_{28} + \dot{E}_D$	$\dot{E}_{36} - \dot{E}_{37} = \dot{E}_{49} - \dot{E}_{48} + \dot{E}_D$
EVA-II	$\dot{E}_{18} - \dot{E}_{19} = \dot{E}_{31} - \dot{E}_{30} + \dot{E}_D$	$\dot{E}_{38} - \dot{E}_{39} = \dot{E}_{541} - \dot{E}_{50} + \dot{E}_D$
SHE-II	$\dot{E}_{23} - \dot{E}_{24} = \dot{E}_{22} - \dot{E}_{21} + \dot{E}_D$	$\dot{E}_{43} - \dot{E}_{44} = \dot{E}_{42} - \dot{E}_{41} + \dot{E}_D$
SP-II	$\dot{E}_{38} = \dot{E}_{21} - \dot{E}_{20} + \dot{E}_D$	$\dot{E}_{60} = \dot{E}_{41} - \dot{E}_{40} + \dot{E}_D$

R-ORC

The R-ORC model is verified by comparing the outcomes to the findings of the same model as presented in Ref. [17]. The state properties for both models are compared in Table 3.7. The comparison of numerous critical performance characteristics obtained from the two models is also included in Table 3.7 along with the related deviation. The results obtained from the current R-ORC model show good agreement with the R-ORC model used in Ref. [17], with a maximum deviation of 1.01%. Therefore, it demonstrates that the code used to simulate the R-ORC in the CPC system configurations produces quite accurate results.

ACS

The validation result of the ACS model is presented in Fig. 3.6. The validation is carried out by comparing the variation of COP with the change in generator temperature at three different evaporator temperatures of 2°C, 5°C, and 10°C for

Table 3.6: Model validation for the GT-HRSG system ($T_{GT,in}$=1520 K, $\eta_{s,AC}$=86%, $\eta_{s,GT}$=86%, $\Delta T_{pp,HRSG}$=30 K, $\dot{W}_{net,GT}$=30 MW).

State	T (K)		P (kPa)		$\dot{m}$ (kg/s)		$\dot{E}$ (MW)	
	Present	Ref. [3]	Present	Ref. [3]	Present	Ref. [3]	Present	Ref. [3]
1	298.15	298.15	101.30	101.30	91.21	91.27	0	0
2	603.31	603.73	1013	1013	91.21	91.27	27.50	27.53
3	850	850	962.35	962.30	91.21	91.27	41.91	41.94
4	1520	1520	914.23	914.20	92.85	92.91	102.56	101.45
5	1006.28	1006.16	109.93	109.90	92.85	92.91	39.76	38.78
6	775.90	779.78	106.63	106.60	92.85	92.91	22.42	21.75
7	422.80	426.89	101.3	101.3	92.85	92.91	2.85	2.77
8	298.15	298.15	2000	2000	14.00	14.00	0.06	0.06
9	485.53	485.57	2000	2000	14.00	14.00	12.82	12.81
10	298.15	298.15	1200	1200	1.64	1.64	84.94	84.99

Parameters	Unit	Present work	Reference work [3]	Deviation (%)
Process heat	MW	37.68	37.75	0.18
Overall energy efficiency	%	52.10	52.16	0.11
Overall exergy efficiency	%	50.33	50.30	0.06
Overall exergy destruction	MW	38.81	39.47	1.70
Overall exergy loss	MW	2.85	2.77	2.80

Table 3.7: Model validation for the R-ORC (P_{VG}=2500 kPa, $T_{COND,in}$=298 K, $T_{COND,out}$=308 K, $\Delta T_{pp,VG}$=10 K, $\dot{Q}_{VG}$=252 kW, Fluid: R123).

State	T (K)		P (kPa)		$\dot{m}$ (kg/s)		$\dot{E}$ (kW)	
	Present	Ref. [17]	Present	Ref. [17]	Present	Ref. [17]	Present	Ref. [17]
1	298.00	298.00	46.57	48.00	1.15	1.15	0	0
2	299.07	299.10	2500.00	2500.00	1.15	1.15	1.96	2.05
3	331.19	328.00	2500.00	2500.00	1.15	1.15	4.74	4.81
4	466.67	468.00	2500.00	2500.00	1.15	1.15	73.73	75.45
5	362.13	365.00	46.57	48.00	1.15	1.15	5.23	5.87
6	326.79	329.00	46.57	48.00	1.15	1.15	1.92	2.00
7	298.00	298.00	100.00	100.00	4.29	4.51	0.00	0.00
8	308.00	308.00	100.00	100.00	4.29	4.51	1.68	1.75

Parameters	Unit	Present work	Reference work [17]	Deviation (%)
Pump work	kW	2.18	2.20	0.91
Net work	kW	53.85	54.30	0.83
Energy efficiency	%	21.56	21.50	0.28
Overall exergy destruction	kW	48.11	49.50	0.29
Exergy efficiency	%	33.56	33.22	1.01

the current ACS model and the ACS model used in Ref. [18]. It is clear from Fig. 3.6 that the outcomes of the current ACS model are in good accord with those of Ref. [18]. Therefore, it validates the accuracy of the ACS model used in the

current work.

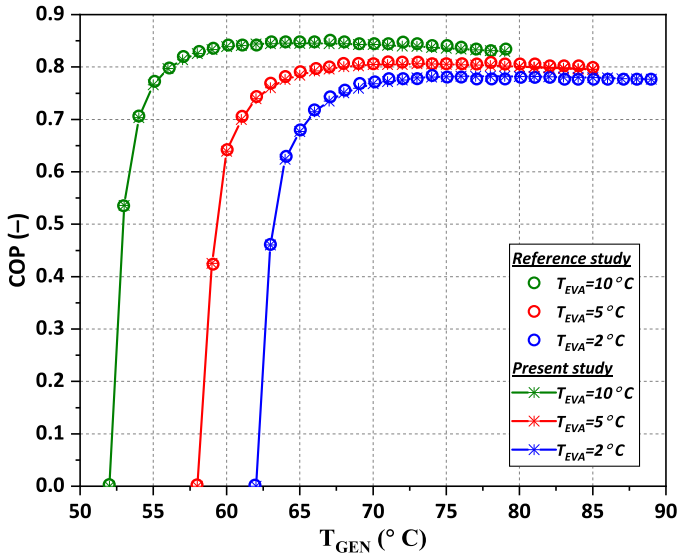

Fig. 3.6: Validation of ACS model with the data reported in Ref. [18].

ST cycle

The validation result of the ST cycle is presented in Fig. 3.7. The validation is carried out by comparing the variation of energy efficiency with the change in ST inlet pressure at three different ST inlet temperatures of 590°C, 500°C, and 400°C for the current ST model and the ST model used in Ref. [4]. It is evident from Fig. 3.7 that the results of the present ST model are in strong accord with those of Ref. [4]. The accuracy of the ST model employed in the current work to simulate the CPC system setup is thus verified.

3.3.2 Energy-based results

The presentation of the properties and mass flow rates at various state points is a standard procedure in the thermodynamic analysis of a system. It not only highlights the mass and property variation across state points in a particular system but also provides relevant data for a comprehensive assessment. Therefore, in this chapter, the state properties for system-I, system-II, system-III and system-IV are shown in Tables 3.8 to 3.11, respectively. It is to be noted that each of the four CPC systems exhibits the same state properties from state 1 to state 4, which are in fact associated with the topping GT cycle. It is because the operating condition of the GT plant is considered the same (refer to Table 3.1) for all four systems. The state properties for states 1-4 are thus only displayed for system-I and not for systems-II

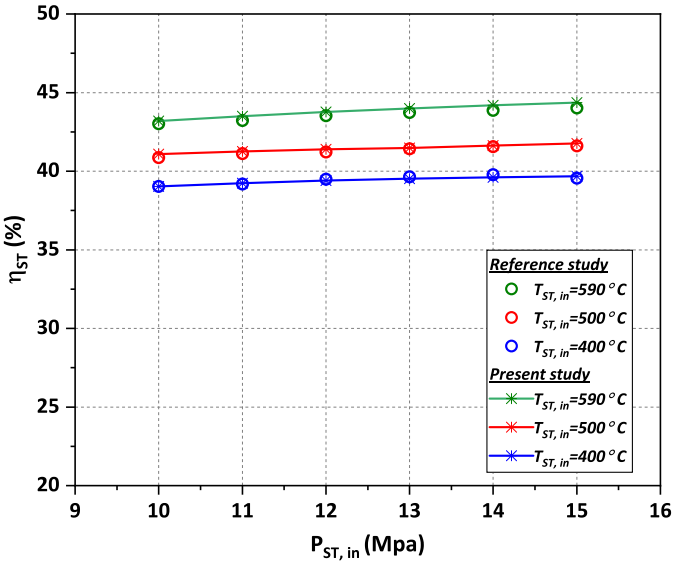

Fig. 3.7: Model validation of ST cycle with the data reported in Ref. [4].

to systems-IV. Tables 3.8 to 3.11 also illustrates that the combustion gas entering the GT has the maximum temperature (1344.71 K) among all streams. The water at the exit of the expansion valve (EV-Ib and EV-IIb) above the evaporator of ACSs (ACS-I and ACS-II), meanwhile, registers the lowest temperature (278.11 K). Similar to this, the AC outlet shows the highest pressure (1013 kPa); while the various state points of the ACSs show the lowest pressure (0.87 kPa). It is also observed that the steam generation rate (16.25 kg/s) is the same for all CPC systems.

The power and cooling outputs and energy conversion efficiencies of the individual subsystems as well as the overall CPC systems are shown in Table 3.12. It is observed that the GT plant in all four CPC systems gives a fixed net power of 31.17 MW. It is also important to note that each of the four systems has a unique ST cycle architecture. Most notably, system-I and system-II employ STs of the back-pressure type, whereas system-III and system-IV employ STs of the condensing type. According to Table 3.12, the condensing type ST produces more power than the back-pressure type ST at the same ST operating condition. Among condensing type STs, the ST cycle corresponding to the system-III generates more power than the ST cycle of the system-IV. Furthermore, among the back-pressure type STs, the power generated by the ST cycle corresponding to system-II generates more power than the ST cycle of system-I.

In system-I, 10.88 kg/s of steam is extracted from ST at a pressure of 500 kPa for driving the R-ORC and the remaining (5.36 kg/s) is further expanded to pass through the ACS-I's generator. In system-II, however, the steam is fully expanded

Table 3.8: Thermodynamic properties at various states of system-I.

States	T	P	$\dot{m}$	h	s	$\dot{E}_{ch}$	$\dot{E}_{ph}$	$\dot{E}$
Units	(K)	(kPa)	(kg/s)	(kJ/kg)	(kJ/kg.K)	(MW)	(MW)	(MW)
1	298.15	101.3	110	341.64	6.91	0.19	0	0.19
2	611.89	1013	110	669.72	6.99	0.19	33.55	33.74
3	1344.71	997.81	110	1744.31	7.92	2.39	106.08	108.46
4	869.83	107.47	112.68	1141.77	8.04	2.39	34.2	36.59
5	505.25	104.34	112.68	718.17	7.42	2.39	7.3	9.68
6	373.15	101.3	112.68	572.9	7.09	2.39	1.82	4.21
7	823.15	8900	16.25	3512.94	6.82	0.81	24.1	24.91
8	459.01	500	10.88	2825.28	7	0.54	8.1	8.64
9	373.15	101.42	5.36	2570.09	7.07	0.27	2.5	2.77
10	373.15	101.42	5.36	419.17	1.31	0.27	0.18	0.45
11	374	8900	5.36	429.35	1.31	0.27	0.23	0.5
12	424.22	485	10.88	636.8	1.85	0.54	0.97	1.51
13	425.38	8900	10.88	646.98	1.86	0.54	1.07	1.62
14	408.55	8900	16.25	575.16	1.68	0.81	1.27	2.08
15	414	1783.59	110.88	458.24	1.7	–	5.63	5.63
16	325.54	109.58	110.88	415.51	1.71	–	0.41	0.41
17	309.3	109.58	110.88	403.87	1.68	–	0.33	0.33
18	303.15	109.58	110.88	230.26	1.1	–	0.01	0.01
19	303.88	1783.59	110.88	231.54	1.11	–	0.13	0.13
20	315.37	1783.59	110.88	243.37	1.14	–	0.18	0.18
21	298.15	101.3	920.94	104.92	0.37	45.99	0	45.99
22	303.15	101.3	920.94	125.82	0.44	45.99	0.16	46.15
23	363.15	5.65	3.74	2669.01	8.66	0.19	0.34	0.53
24	308.15	5.65	3.74	146.63	0.51	0.19	0	0.19
25	278.11	0.87	3.74	146.63	0.53	0.19	-0.02	0.16
26	278.15	0.87	3.74	2510.06	9.02	0.19	-0.66	-0.47
27	308.15	0.87	24.5	85.32	0.21	5.02	0.01	5.03
28	308.15	5.65	24.5	85.32	0.21	5.02	0.01	5.03
29	338.84	5.65	24.5	146.89	0.41	5.02	0.11	5.12
30	363.15	5.65	20.76	242.41	0.47	6.23	0.18	6.41
31	321.9	5.65	20.76	169.74	0.26	6.23	-0.01	6.22
32	321.9	0.87	20.76	169.74	0.26	6.23	-0.01	6.22
33	298.15	101.3	517.89	104.92	0.37	25.87	0	25.87
34	303.15	101.3	517.89	125.82	0.44	25.87	0.09	25.96
35	298.15	101.3	451.51	104.92	0.37	22.55	0	22.55
36	303.15	101.3	451.51	125.82	0.44	22.55	0.08	22.63
37	288.15	101.3	421.94	63.08	0.22	21.07	0.3	21.38
38	283.15	101.3	421.94	42.12	0.15	21.07	0.69	21.76
39	363.15	5.65	5.31	2669.01	8.66	0.27	0.48	0.75
40	308.15	5.65	5.31	146.63	0.51	0.27	0	0.27

Table 3.8: Thermodynamic properties at various states of system-I (continued).

States	T	P	$\dot{m}$	h	s	$\dot{E}_{ch}$	$\dot{E}_{ph}$	$\dot{E}$
Units	(K)	(kPa)	(kg/s)	(kJ/kg)	(kJ/kg.K)	(MW)	(MW)	(MW)
41	278.11	0.87	5.31	146.63	0.53	0.27	-0.03	0.23
42	278.15	0.87	5.31	2510.06	9.02	0.27	-0.94	-0.67
43	308.15	0.87	34.77	85.32	0.21	7.12	0.02	7.14
44	308.15	5.65	34.77	85.32	0.21	7.12	0.02	7.14
45	338.84	5.65	34.77	146.89	0.41	7.12	0.15	7.27
46	363.15	5.65	29.46	242.41	0.47	8.84	0.25	9.1
47	321.9	5.65	29.46	169.74	0.26	8.84	-0.02	8.83
48	321.9	0.87	29.46	169.74	0.26	8.84	-0.02	8.83
49	298.15	101.3	735.05	104.92	0.37	36.71	0	36.71
50	303.15	101.3	735.05	125.82	0.44	36.71	0.13	36.84
51	298.15	101.3	640.84	104.92	0.37	32.01	0	32.01
52	303.15	101.3	640.84	125.82	0.44	32.01	0.11	32.12
53	288.15	101.3	598.87	63.08	0.22	29.91	0.43	30.34
54	283.15	101.3	598.87	42.12	0.15	29.91	0.98	30.89
55	333.35	2650	2.68	946.87	5.10	134.3	0	134.3

up to a pressure of 257.80 kPa before being passed through the VG. It is also observed that a pressure drop of 3% is considered across the VG. Moreover, Table 3.12 also shows that the powers produced by the R-ORCs in system-I and system-II are 4.50 MW and 6.09 MW, respectively. The total power generated by systems is determined by adding the net powers of the GT cycle, ST cycle and R-ORC. It is found that system-III delivers the highest total power of 49.98 MW followed by system-II with 49.76 MW. Meanwhile, the total power generated by system-IV is the next in order with 48.69 MW followed by system-I with 47.80 MW.

Additionally,Table 3.12 shows that system-I, out of the four systems, delivers the maximum cooling load of 21.40 MW, followed by system-IV with a cooling load of 20.16 MW. It is obvious because, among the four systems, system-I and system-IV are the only systems that are incorporated with two ACSs (ACS-I and ACS-II). The ACS-I is a steam-operated absorption chiller that supplies a cooling load of 8.84 MW and 8.25 MW in systems-I and system-IV, respectively. The gas-operated absorption chiller (ACS-II), on the other hand, produces a cooling load of 12.55 MW, 12.34 MW, 11.80 MW, and 11.91 MW in system-I to system-IV, respectively. It is quite apparent that in the proposed CPC systems, ACS-II delivers a much higher cooling load as compared to ACS-I. This is because the heat provided by the exhaust gas to the ACS-II generator is significantly more than the heat supplied by the steam to the ACS-I generator. Additionally, the individual cooling loads of the

Table 3.9: Thermodynamic properties at various states of system-II.

States	T	P	$\dot{m}$	h	s	$\dot{E}_{ch}$	$\dot{E}_{ph}$	$\dot{E}$
Units	(K)	(kPa)	(kg/s)	(kJ/kg)	(kJ/kg.K)	($/h)	($/h)	($/h)
5	501.42	104.34	112.68	713.91	7.41	2.39	7.1	9.49
6	373.15	101.3	112.68	572.9	7.09	2.39	1.82	4.21
7	823.15	8900	16.25	3512.94	6.82	0.81	24.1	24.91
8	401.62	257.8	16.25	2717.99	7.04	0.81	10.12	10.93
9	400.57	250.07	16.25	535.38	1.61	0.81	0.99	1.8
10	401.59	8900	16.25	545.62	1.61	0.81	1.14	1.95
11	396.55	1282.75	169.15	451.22	1.69	–	7.63	7.63
12	322.81	109.58	169.15	413.54	1.71	–	0.59	0.59
13	308.45	109.58	169.15	403.27	1.68	–	0.5	0.5
14	303.15	109.58	169.15	230.26	1.1	–	0.01	0.01
15	303.66	1282.75	169.15	231.16	1.11	–	0.15	0.15
16	313.78	1282.75	169.15	241.57	1.14	–	0.21	0.21
17	298.15	101.3	1400.1	104.92	0.37	69.93	0	69.93
18	303.15	101.3	1400.1	125.82	0.44	69.93	0.24	70.17
19	363.15	5.65	5.2	2669.01	8.66	0.26	0.47	0.73
20	308.15	5.65	5.2	146.63	0.51	0.26	0	0.26
21	278.11	0.87	5.2	146.63	0.53	0.26	-0.03	0.23
22	278.15	0.87	5.2	2510.06	9.02	0.26	-0.92	-0.66
23	308.15	0.87	34.09	85.32	0.21	6.98	0.02	7
24	308.15	5.65	34.09	85.32	0.21	6.98	0.02	7
25	338.84	5.65	34.09	146.89	0.41	6.98	0.15	7.13
26	363.15	5.65	28.89	242.41	0.47	8.67	0.25	8.92
27	321.9	5.65	28.89	169.74	0.26	8.67	-0.02	8.65
28	321.9	0.87	28.89	169.74	0.26	8.67	-0.02	8.65
29	298.15	101.3	720.58	104.92	0.37	35.99	0	35.99
30	303.15	101.3	720.58	125.82	0.44	35.99	0.12	36.11
31	298.15	101.3	628.23	104.92	0.37	31.38	0	31.38
32	303.15	101.3	628.23	125.82	0.44	31.38	0.11	31.49
33	288.15	101.3	587.08	63.08	0.22	29.32	0.42	29.74
34	283.15	101.3	587.08	42.12	0.15	29.32	0.96	30.28
35	333.35	2650	2.68	946.87	5.10	134.3	0	134.3

ACS-I and ACS-II are added to determine the net cooling output of each system. Similarly, by combining the net power and cooling loads of each system, the net energy output is obtained. It is observed that system-I delivers the maximum net energy output of 69.20 MW, followed by systems-IV, system-II, and system-III, with net energy outputs of 68.86 MW, 62.06 MW, and 61.78 MW, respectively.

Further, Table 3.12 shows that for all four CPC systems, the energy efficiency of the topping GT cycle is 24.10%. Meanwhile, the energy efficiency of the ST cycle is

Table 3.10: Thermodynamic properties at various states of system-III.

States	T	P	$\dot{m}$	h	s	$\dot{E}_{ch}$	$\dot{E}_{ph}$	$\dot{E}$
Units	(K)	(kPa)	(kg/s)	(kJ/kg)	(kJ/kg.K)	(MW)	(MW)	(MW)
5	497.44	104.34	112.68	709.49	7.4	2.39	6.9	9.29
6	373.15	101.3	112.68	572.9	7.09	2.39	1.82	4.21
7	823.15	8900	16.25	3512.94	6.82	0.81	24.1	24.91
8	393.36	200	2.09	2679.13	7.06	0.1	1.21	1.32
9	316.91	9	14.15	2268.43	7.2	0.71	1.78	2.49
10	316.91	9	14.15	183.25	0.62	0.71	0.03	0.74
11	316.92	200	14.15	183.47	0.62	0.71	0.03	0.74
12	393.36	200	16.25	504.7	1.53	0.81	0.86	1.67
13	394.33	8900	16.25	514.94	1.53	0.81	1.02	1.83
14	298.15	101.3	1000.80	104.92	0.37	50.38	0	50.38
15	305.15	101.3	1000.80	134.18	0.46	50.38	0.34	50.72
16	363.15	5.65	4.99	2669.01	8.66	0.25	0.45	0.7
17	308.15	5.65	4.99	146.63	0.51	0.25	0	0.25
18	278.11	0.87	4.99	146.63	0.53	0.25	-0.03	0.22
19	278.15	0.87	4.99	2510.06	9.02	0.25	-0.88	-0.63
20	308.15	0.87	32.7	85.32	0.21	6.69	0.02	6.71
21	308.15	5.65	32.7	85.32	0.21	6.69	0.02	6.71
22	338.84	5.65	32.7	146.89	0.41	6.69	0.14	6.83
23	363.15	5.65	27.7	242.41	0.47	8.31	0.24	8.55
24	321.9	5.65	27.7	169.74	0.26	8.31	-0.02	8.3
25	321.9	0.87	27.7	169.74	0.26	8.31	-0.02	8.3
26	298.15	101.3	691.12	104.92	0.37	34.52	0	34.52
27	303.15	101.3	691.12	125.82	0.44	34.52	0.12	34.64
28	298.15	101.3	602.55	104.92	0.37	30.09	0	30.09
29	303.15	101.3	602.55	125.82	0.44	30.09	0.1	30.2
30	288.15	101.3	563.08	63.08	0.22	28.12	0.4	28.53
31	283.15	101.3	563.08	42.12	0.15	28.12	0.92	29.04
32	333.35	2650	2.68	946.87	5.10	134.3	0	134.3

highest for system-III with 38.61% followed by system-IV with 35.97%. The energy efficiencies of the ST cycles in systems-I and system-II, however, are significantly low, at 25.41% and 25.91%, respectively. It suggests that the condensing-type ST cycle has a higher energy efficiency than the back-pressure-type ST cycle. It is because, in the condensing-type ST cycle, the steam is expended fully up to condenser pressure thus generates more power.The back-pressure type ST cycle produces less power because the steam is expanded to a pressure that is much higher than the typical condenser pressure. Next, the energy efficiency of the R-ORC in system-I and system-II are found to be 18.90% and 17.19%, respectively. It is noteworthy that the R-ORC in system-I has a greater energy efficiency despite producing less power

than the R-ORC in system-II. It is because, in system-I, the R-ORC receives 23.82 MW of waste heat out of which 4.50 MW is converted into power. On the other hand, in system-II, the R-ORC receives 35.46 MW of waste heat out of which 6.09 MW is converted into power. Meanwhile, the COP of ACSs (ACS-I and ACS-II), which is the same for all four CPC systems, is 0.774. This is because the COP of an ACS only depends on the component temperatures and SHE effectiveness which are fixed for all ACSs integrated into the four CPC systems. Finally, the overall energy efficiency of the four CPC systems is calculated, and it is found that system-I has the highest energy efficiency at 56.31%, followed by system-IV (56.03%). Moreover, System-II and system-III are estimated to have overall energy efficiencies of 47.98% and 47.76%, respectively.

3.3.3 Exergy-based results

The physical exergy, chemical exergy and total exergy rates at each state point for system-I to system-IV, are shown in Tables 3.8 to 3.11, respectively. The stream entering the GT in all four configurations is found to have the highest physical exergy rate (108.46 MW). The same observation was made in Ref. [9] for a GT-based CHP plant. The large temperature difference of 1071.60 K between the combustion gas (T_3=1344.71 K) and dead state (T_0=298.15 K) results in a very high physical exergy rate. Further, the physical exergy rates are found to be negative at state points corresponding to the inlet and outlet of evaporators as well as across the expansion valves of the ACSs. Particularly for system-I, the physical exergy at the inlet (state 25) and outlet (state 26) of the evaporator (EVA-I) is negative because the temperature (278.11 K) and pressure (0.87 kPa) at those sites are lower than the dead state temperature (298.15 K) and pressure (101.15 kPa). The physical exergy across the expansion valve (EV-Ib) (states 31 and 32) is negative because, despite the higher temperatures (321.9 K) there than in the dead state, the pressure is lower (5.65 and 0.87 kPa) than the dead state pressure. The same is the case with ACS-II of the system-I as well as other ACSs of the remaining systems (system-II, system-III and system-IV). Besides, the fuel stream has the highest value of chemical exergy rate of 134.30 MW in all four systems.

The exergy parameters of each component of systems-I and system-II are shown in Table 3.13. Similarly, the exergy parameters of each component of systems-III and system-IV are shown in Table 3.14. It is observed that the exergy destruction rates of the GT plant's components are the same across all four CPC systems. It is because the operating conditions and the layouts of the topping GT plant are the

Table 3.11: Thermodynamic properties at various states of system-IV.

States	T	P	$\dot{m}$	h	s	$\dot{E}_{ch}$	$\dot{E}_{ph}$	$\dot{E}$
Units	(K)	(kPa)	(kg/s)	(kJ/kg)	(kJ/kg.K)	(MW)	(MW)	(MW)
5	497.44	104.34	112.68	709.49	7.4	2.39	6.9	9.29
6	373.15	101.3	112.68	572.9	7.09	2.39	1.82	4.21
7	823.15	8900	16.25	3512.94	6.82	0.81	24.1	24.91
8	393.36	200	1.62	2679.13	7.06	0.08	0.94	1.02
9	373.15	101.42	4.94	2576.48	7.09	0.25	2.31	2.56
10	316.91	9	9.68	2266.88	7.2	0.48	1.22	1.7
11	316.91	9	9.68	183.25	0.62	0.48	0.02	0.51
12	316.92	200	9.68	183.47	0.62	0.48	0.02	0.51
13	373.15	101.42	4.94	419.17	1.31	0.25	0.17	0.41
14	373.16	200	4.94	419.28	1.31	0.25	0.17	0.41
15	335.96	200	14.62	263.1	0.87	0.73	0.14	0.87
16	393.36	200	16.25	504.7	1.53	0.81	0.86	1.67
17	394.33	8900	16.25	514.94	1.53	0.81	1.02	1.83
18	298.15	101.3	689.63	104.92	0.37	34.44	0	34.44
19	305.15	101.3	689.63	134.18	0.46	34.44	0.23	34.68
20	363.15	5.65	3.49	2669.01	8.66	0.17	0.32	0.49
21	308.15	5.65	3.49	146.63	0.51	0.17	0	0.18
22	278.11	0.87	3.49	146.63	0.53	0.17	-0.02	0.15
23	278.15	0.87	3.49	2510.06	9.02	0.17	-0.61	-0.44
24	308.15	0.87	22.85	85.32	0.21	4.68	0.01	4.69
25	308.15	5.65	22.85	85.32	0.21	4.68	0.01	4.69
26	338.84	5.65	22.85	146.89	0.41	4.68	0.1	4.78
27	363.15	5.65	19.36	242.41	0.47	5.81	0.17	5.98
28	321.90	5.65	19.36	169.74	0.26	5.81	-0.01	5.8
29	321.90	0.87	19.36	169.74	0.26	5.81	-0.01	5.8
30	298.15	101.3	483.1	104.92	0.37	24.13	0	24.13
31	303.15	101.3	483.1	125.82	0.44	24.13	0.08	24.21
32	298.15	101.3	421.19	104.92	0.37	21.04	0	21.04
33	303.15	101.3	421.19	125.82	0.44	21.04	0.07	21.11
34	288.15	101.3	393.6	63.08	0.22	19.66	0.28	19.94
35	283.15	101.3	393.6	42.12	0.15	19.66	0.64	20.3
36	363.15	5.65	5.04	2669.01	8.66	0.25	0.46	0.71
37	308.15	5.65	5.04	146.63	0.51	0.25	0	0.25
38	278.11	0.87	5.04	146.63	0.53	0.25	-0.03	0.22
39	278.15	0.87	5.04	2510.06	9.02	0.25	-0.89	-0.64

same in all four configurations. The CC has the highest irreversibility among the GT cycle components, with a exergy destruction rate of 59.57 MW, followed by the GT and AC. In fact, among all the components of the CPC systems, CC has the highest exergy destruction rate. As can be seen from Table 3.13 and Table 3.14, CC alone

Table 3.11: Thermodynamic properties at various states of system-IV (continued).

States	T	P	$\dot{m}$	h	s	$\dot{E}_{ch}$	$\dot{E}_{ph}$	$\dot{E}$
Units	(K)	(kPa)	(kg/s)	(kJ/kg)	(kJ/kg.K)	(MW)	(MW)	(MW)
40	308.15	0.87	33.02	85.32	0.21	6.76	0.02	6.78
41	308.15	5.65	33.02	85.32	0.21	6.76	0.02	6.78
42	338.84	5.65	33.02	146.89	0.41	6.76	0.14	6.9
43	363.15	5.65	27.98	242.41	0.47	8.4	0.24	8.64
44	321.9	5.65	27.98	169.74	0.26	8.4	-0.02	8.38
45	321.9	0.87	27.98	169.74	0.26	8.4	-0.02	8.38
46	298.15	101.3	697.98	104.92	0.37	34.86	0	34.86
47	303.15	101.3	697.98	125.82	0.44	34.86	0.12	34.98
48	298.15	101.3	608.52	104.92	0.37	30.39	0	30.39
49	303.15	101.3	608.52	125.82	0.44	30.39	0.11	30.5
50	288.15	101.3	568.66	63.08	0.22	28.4	0.41	28.81
51	283.15	101.3	568.66	42.12	0.15	28.4	0.93	29.33
52	333.35	2650	2.68	946.87	5.10	134.3	0	134.3

Table 3.12: Energy outputs of the four CPC systems.

Parameters	Units	System-I	System-II	System-III	System-IV
Net GT power	MW	31.17	31.17	31.17	31.17
Net ST power	MW	12.13	12.49	18.81	17.52
Net R-ORC power	MW	4.50	6.09	–	–
Net power	MW	47.80	49.76	49.98	48.69
ACS-I cooling output	MW	8.84	–	–	8.25
ACS-II cooling output	MW	12.55	12.34	11.80	11.91
Net cooling output	MW	21.40	12.34	11.80	20.16
Net output energy	MW	69.20	62.06	61.78	68.86
Net input energy	MW	122.88	122.88	122.88	122.88
Energy efficiency of GT cycle	%	24.10	24.10	24.10	24.10
Energy efficiency of ST cycle	%	25.41	25.91	38.61	35.97
Energy efficiency of R-ORC	%	18.90	17.19	–	–
COP of ACS-I	–	0.774	–	–	0.774
COP of ACS-II	–	0.774	0.774	0.774	0.774
Overall energy efficiency	%	56.31	50.51	50.27	56.03

accounts for 73.66% of the overall exergy destruction rate corresponding to system-I. The CC accounts for 74.96%, 75.23%, and 77.09% of the total exergy destruction in system-II, system-III, and system-IV, respectively. Chemical reaction, heat transfer through finite temperature difference, and fluid friction are the main contributors to irreversibility, with chemical reaction being the dominant factor. The presence of all three factors in the CC leads to substantial exergy destruction.

The GT is the next major component responsible for significant exergy destruc-

Table 3.13: Component wise exergy performance parameters of systems-I and II.

	System-I			System-II		
Components	$\dot{E}_D$ (MW)	Y_D (%)	ε (%)	$\dot{E}_D$ (MW)	Y_D (%)	ε (%)
AC	2.54	3.14	92.95	2.54	3.2	92.95
CC	59.57	73.66	64.55	59.57	74.96	64.55
GT	4.61	5.70	93.58	4.61	5.81	93.58
HRSG	4.07	5.04	84.86	4.14	5.21	84.72
ST	1.21	1.49	91.06	1.32	1.66	90.56
FP-I	≈ 0	≈ 0	92.99	0.01	0.02	92.57
FP-II	≈ 0	≈ 0	92.03	0.01	0.02	90.18
FP-III	0.01	0.02	90.19	–	–	–
VG	1.68	2.08	76.39	1.71	2.15	81.25
VT	0.58	0.72	88.92	0.78	0.99	88.85
IHE	0.03	0.04	62.08	0.04	0.04	62.75
COND	0.16	0.2	49.53	0.25	0.31	49.72
GEN-I	0.5	0.62	78.28	–	–	–
ABS-I	0.63	0.77	12.53	–	–	–
CON-I	0.26	0.32	23.13	–	–	–
EVA-I	0.25	0.31	60.91	–	–	–
SHE-I	0.1	0.12	48.05	–	–	–
GEN-II	2.90	3.59	47.03	2.76	3.47	47.81
ABS-II	0.89	1.1	12.53	0.87	1.1	12.53
CON-II	0.37	0.46	23.13	0.36	0.46	23.13
EVA-II	0.35	0.44	60.91	0.35	0.44	60.91
SHE-II	0.14	0.17	48.05	0.14	0.17	48.05
Overall	80.08	–	36.29	79.47	–	37.45

tion in all four CPC systems. The exergy destruction rate of GT in all four systems is 4.61 MW. Moreover, the exergy destruction ratios of GT in system-I, system-II, system-III and system-IV are 5.7%, 5.81%, 5.83% and 5.97%, respectively. The fluid friction that occurs when combustion gas impinges on the turbine blades is the primary cause of exergy destruction in the GT. Among all the components of the four CPC systems, the HRSG has the third-highest rate of exergy destruction. The HRSG's high rate of exergy destruction is caused by fluid friction and heat transfer, with stream-to-stream heat transfer being the dominant contributor. The GEN-II appears next in the list, followed by AC and ST. The irreversibilities generated by the heat transfer between the flue gas and the LiBr-H_2O solution and the separation of H_2O from the LiBr-H_2O solution are the source of the substantial exergy destruction in GEN-II. Meanwhile, the exergy destruction rate of AC in all four systems is 2.54 MW. The exergy destruction rates of ST in system-I, system-II, system-III and system-IV are 1.21 MW, 1.32 MW, 2.13 MW and 1.95 MW, respectively with

Table 3.14: Component wise exergy performance parameters of systems-III and IV.

	System-III			System-IV		
Components	$\dot{E}_D$ (MW)	Y_D (%)	ε (%)	$\dot{E}_D$ (MW)	Y_D (%)	ε(%)
AC	2.54	3.21	92.95	2.54	3.17	92.95
CC	59.57	75.23	64.55	59.57	74.48	64.55
GT	4.61	5.83	93.58	4.61	5.76	93.58
HRSG	4.22	5.33	84.55	4.22	5.27	84.55
ST	2.13	2.69	89.9	1.95	2.43	90.09
FP-I	0.01	0.02	92.44	0.01	0.02	92.44
FP-II	≈ 0	≈ 0	90.59	≈ 0	≈ 0	90.59
FP-III	–	–	–	≈ 0	≈ 0	92.01
OWH	0.38	0.48	81.3	0.22	0.27	88.56
COND	1.41	1.78	19.52	0.96	1.20	19.52
GEN-I	–	–	–	0.45	0.56	79.05
ABS-I	–	–	–	0.58	0.73	12.53
CON-I	–	–	–	0.24	0.30	23.13
EVA-I	–	–	–	0.23	0.29	60.91
SHE-I	–	–	–	0.09	0.12	48.05
GEN-II	2.66	3.36	47.67	2.63	3.29	48.14
ABS-II	0.84	1.06	12.53	0.84	1.05	12.53
CON-II	0.35	0.44	23.13	0.35	0.44	23.13
EVA-II	0.33	0.42	60.91	0.33	0.42	60.91
SHE-II	0.13	0.17	48.05	0.13	0.16	48.05
Overall	79.19	–	37.60	79.98	–	36.91

the respective exergy destruction ratios of 1.49%, 1.66%, 2.69% and 2.52%. It is interesting to note that the exergy destruction rates in the condensing type STs (system-III and system-IV) are higher than that of back-pressure type STs (system-I and system-II). It is because, in the condensing type STs, the steam is expanded up to a very low pressure (condenser pressure) which results in higher irreversibilities associated with the fluid friction.

Table 3.13 and Table 3.14 also shows that among all the components of four CPC systems, FPs (FP-I, FP-II and FP-III) have the comparatively least exergy destruction rate. In fact, the solution pumps (SPs) employed in the ACSs have even lower exergy destruction and hence the exergy results of SPs are not shown in Table 3.13 and Table 3.14. It is also worth noting that CONDs shown in Table 3.13 correspond to R-ORC of the system-I and system-II. On the other hand, the CONDs shown in Table 3.14 correspond to the ST cycle of the system-III and system-IV. It is interesting to observe that the exergy destruction in CONDs of R-ORCs (system-I and system-II) is significantly less than that of the CONDs of the ST cycle (system-

III and system-IV). The dominating factor of irreversibility in COND is heat transfer through a finite temperature difference. The temperature difference between the working fluid and the cooling water is greater in CONDs of the ST cycle than it is in CONDs of the R-ORC and it leads to higher exergy destruction of CONDs of the ST cycle. Meanwhile, the OWH in system-III has an exergy destruction rate of 0.38 MW with an exergy destruction ratio of 0.48%. On the other hand, the OWH in system-IV has an exergy destruction rate of 0.22 MW with an exergy destruction ratio of 0.28%. The OWH in system-III has a comparatively higher exergy destruction rate than the OWH in system-IV. It is because the mass flow rate of extracted steam entering the OWH is higher in system-III (2.09 kg/s) as compared to system-IV (1.62 kg/s).

It is intriguing to note that the components of ACS-I show the same pattern of exergy destruction in all four systems. The largest rate of exergy destruction among the ACS-I components is incurred by ABS-I, followed by GEN-I, CON-I, EVA-I, and SHE-I. The same observation was made in one of the previous study [22]. It is also observed that the magnitude of exergy destruction in the respective components of ACS-I in system-I is higher than that of system-IV. It is justified because the cooling load provided by the ACS-I in system-I (8.84 MW) is higher than that of system-IV (8.25 MW). Meanwhile, the largest rate of exergy destruction among the ACS-II components is incurred by GEN-II, followed by ABS-II, CON-II, EVA-II, and SHE-II. In fact, some studies [6, 8] also found that the GEN is the main source of exergy destruction in the ACS. Therefore, whether GEN or ABS will have the maximum irreversibility in an ACS relies on the energy quality of the heat source and the operational conditions of the system. Moreover, Table 3.13 and Table 3.14 also show that the overall exergy destruction of system-I is the highest (80.08 MW) and that of system-III is the lowest (79.19 MW).

Table 3.13 and Table 3.14 also shows the exergy efficiency of each component of the four systems. It is observed that GT is the most efficient component in all four systems with the highest exergy efficiency of 93.58%. The next most efficient component is the AC with an exergy efficiency of 92.95%. In the topping GT plant, the CC has the least exergy efficiency of 64.55%. It is justified because, in the CC, the majority of the fuel exergy is destroyed due to the presence of irreversibilities, which ultimately lowers the exergy efficiency. A general observation can also be drawn from Table 3.13 and Table 3.14 that the heat exchangers have lower exergy efficiency. For instance, the condenser, IHE and all the components of ACSs show very poor exergy efficiency. In fact, the absorber of ACS-II shows the least exergy

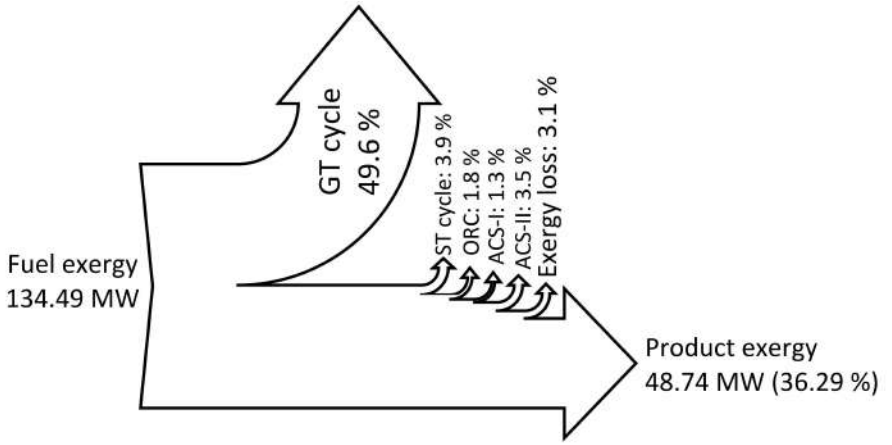

(a) system-I

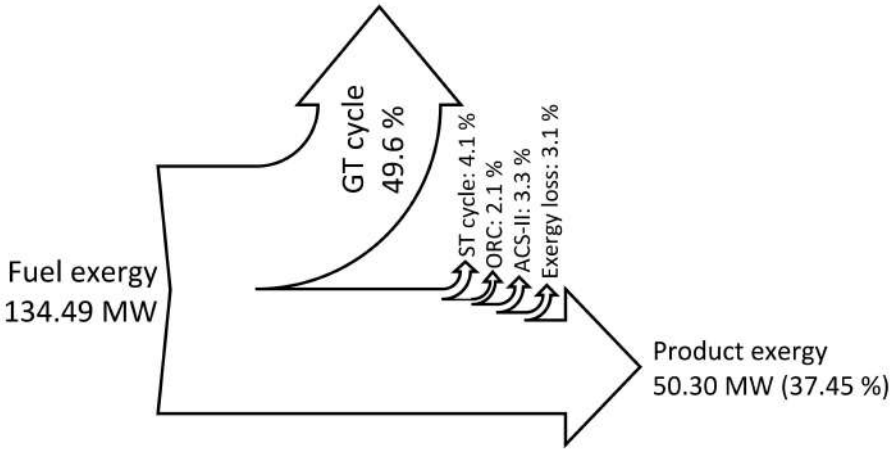

(b) system-II

Fig. 3.8: Exergy flow diagram of CPC systems.

efficiency of 12.53% in all four systems.

The four CPC systems are also analyzed subsystem-wise using exergy flow diagrams. The exergy flow diagram, as the name implies, depicts the flow of exergy in a system. It provides a clear picture of how much exergy enters the system as fuel exergy and how much the given system is capable of converting the fuel exergy into product exergy. Exergy destruction and exergy loss are determined by the difference between fuel and product exergy. The exergy flow diagram for system-I to system-IV is shown in Figs. 3.8(a) to 3.9(b). It is observed that the fuel exergy rate (134.49 MW) for all four CPC systems is the same. Also, the GT plant alone is responsible for the destruction of 49.60% of the fuel exergy. The next major contributor in terms of subsystems is the ST cycle. It is seen that the percentage of fuel exergy destroyed in the ST cycle associated with system-I to system-IV are 3.9%, 4.1%, 6.1% and 5.5%, respectively. It is also observed that the ST cycle in system-III and

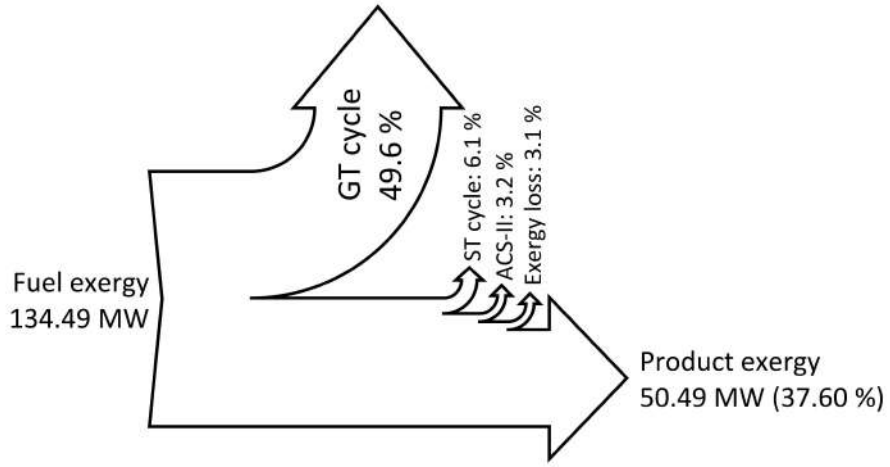

(a) system-III

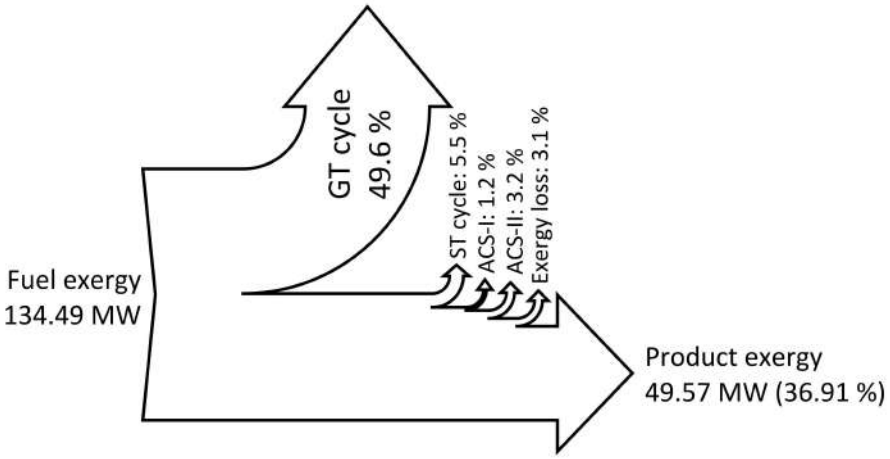

(b) system-IV

Fig. 3.9: Exergy flow diagram of CPC systems.

system-IV have higher exergy destruction as compared to the ST cycles of system-I and system-II. It is because the ST cycles in system-III and system-IV include a condensing type of ST with OWH and COND whereas the ST cycles in system-I and system-II include a back pressure ST. Moreover, it is already discussed that back pressure ST has lower exergy destruction than the condensing type of ST. The ACS-II is the next biggest contributor, causing the respective exergy destruction of 3.5%, 3.3%, 3.2%, and 3.2% of fuel exergy in system-I to system-IV. Then in system-I and system-II, the percentage of fuel exergy destroyed in R-ORC is 1.8% and 2.1%, respectively. Similarly, in system-I and system-IV, the percentage of fuel exergy destroyed in ACS-I is 1.3% and 1.2%, respectively. It is also interesting to note that in all four systems, around 3.1% (4.21 MW) of fuel exergy is lost to the environment along with the exhaust gas. The exergy flow diagram also shows that

the product exergy obtained from system-I to system-IV is 48.74 MW, 50.30 MW, 50.49 MW and 49.57 MW, respectively. Similarly, the exergy efficiency for each system is also shown in the exergy flow diagrams. Around 36.29% of fuel exergy is converted into the produce exergy by the system-I. Likewise, the exergy efficiency of system-II to system-IV is 37.45%, 37.60% and 36.91%, respectively.

3.4 Summary

In this chapter, four configurations of GT-based combined power and cooling systems are proposed. The systems are configured based on the integration of the simple GT plant with the bottoming cycle that includes the steam turbine cycle, Recuperative organic Rankine cycle and absorption cooling systems. The performances of the proposed systems are evaluated using energy and exergy analyses. The main findings obtained from this study are presented below:

- The topping GT plant gives a net power of 31.17 MW in all four CPC system configurations with an energy conversion efficiency of 24.10%.
- The condensing type ST gives significantly higher power as compared to the back-pressure type ST for the same operating condition. The back-pressure type ST in system-I and system-II generate a net power of 12.13 MW and 12.49 MW, respectively. On the other hand, the condensing type ST in system-III and system-IV generates a net power of 18.81 MW and 17.52 MW, respectively.
- When comparing the CPC systems using energy analysis, system-I is found to be the best system, having the highest net energy output of 69.20 MW (47.80 MW is the power output and 21.40 MW is the cooling output) and the highest energy efficiency of 56.31%.
- The CC is the component with the highest irreversibility accounting for more than 70% of the overall exergy destruction of the respective systems. The combustion reaction, heat transfer and fluid friction are the sources of irreversibilities in the CC.
- The GT is the most efficient component in all four systems with the highest exergy efficiency of 93.58%. It implies that the GT could convert the fuel exergy fed to it into product exergy with the highest efficiency. In the topping GT plant, the CC has the least exergy efficiency of 64.55%. It is justified

because, in the CC, the majority of the fuel exergy is destroyed due to the presence of irreversibilities, which ultimately lowers the exergy efficiency.

- The exergy flow diagram shows that the GT plant alone is responsible for the destruction of 49.60% of the fuel exergy in all four systems. It is also observed that around 3.1% (4.21 MW) of fuel exergy is lost to the environment along with the exhaust gas in all four systems.

- According to exergy analysis, system-III outperforms the other CPC system configurations. It is because system-III has the least overall exergy destruction rate of 79.19 MW and consequently the highest exergy efficiency of 37.60%.

According to this study, system-I outperforms the remaining systems based on energy analysis, whereas system-III outperforms the remaining systems based on exergy analysis. It highlights the crucial fact that just because an energy conversion system exhibits superior performance based on energy analysis does not mean that the performance of the system will be the same based on exergy analysis. However, this also does not ensure that the system-III will also be the most cost effective and environment friendly. Moreover, in this study, the performance of all the systems is evaluated at a fixed base case condition. Therefore, the suggested systems could even perform better at their optimal operating conditions obtained through optimization. Further, the performance of the proposed systems could also be improved by incorporating some architectural modifications in the present layouts. The upcoming chapters will deal with the issues discussed above.

Bibliography

[1] Alijanpour sheshpoli, M., Mousavi Ajarostaghi, S. S., and Delavar, M. A. Waste heat recovery from a 1180kW proton exchange membrane fuel cell (PEMFC) system by Recuperative organic Rankine cycle (RORC). *Energy*, 157:353–366, 2018.

[2] Anvari, S., Jafarmadar, S., and Khalilarya, S. Proposal of a combined heat and power plant hybridized with regeneration organic Rankine cycle: Energy-Exergy evaluation. *Energy Conversion and Management*, 122:357–365, 2016.

[3] Bejan, Adrian, George Tsatsaronis and Moran., M. J. *Thermal design and optimization*. John Wiley Sons, New York, 1995.

[4] Dincer, I. and Al-Muslim, H. Thermodynamic analysis of reheat cycle steam power plants. *International Journal of Energy Research*, 25(8):727–739, 2001.

[5] Ding, P., Liu, X., Qi, H., Shen, H., Liu, X., and Farkoush, S. G. Multi-objective optimization of a new cogeneration system driven by gas turbine cycle for power and freshwater production. *Journal of Cleaner Production*, 288:125639, 2021.

[6] Gogoi, T. K. and Talukdar, K. Exergy based parametric analysis of a combined reheat regenerative thermal power plant and water–LiBr vapor absorption refrigeration system. *Energy Conversion and Management*, 83:119–132, 2014.

[7] J. Souza, R., Dos Santos, C. A., Ochoa, A. A., Marques, A. S., L. M. Neto, J., and Michima, P. S. Proposal and 3E (energy, exergy, and exergoeconomic) assessment of a cogeneration system using an organic Rankine cycle and an Absorption Refrigeration System in the Northeast Brazil: Thermodynamic investigation of a facility case study. *Energy Conversion and Management*, 217: 113002, 2020.

[8] Khaliq, A. Exergy analysis of gas turbine trigeneration system for combined production of power heat and refrigeration. *International Journal of Refrigeration*, 32(3):534–545, 2009.

[9] Khaljani, M., Khoshbakhti Saray, R., and Bahlouli, K. Comprehensive analysis of energy, exergy and exergo-economic of cogeneration of heat and power in a combined gas turbine and organic Rankine cycle. *Energy Conversion and Management*, 97:154–165, 2015.

[10] Khaljani, M., Khoshbakhti Saray, R., and Bahlouli, K. Comprehensive analysis of energy, exergy and exergo-economic of cogeneration of heat and power in a combined gas turbine and organic Rankine cycle. *Energy Conversion and Management*, 97:154–165, 2015.

[11] Kianfard, H., Khalilarya, S., and Jafarmadar, S. Exergy and exergoeconomic evaluation of hydrogen and distilled water production via combination of PEM electrolyzer, RO desalination unit and geothermal driven dual fluid ORC. *Energy Conversion and Management*, 177:339–349, 2018.

[12] Kotas, T. J. *The exergy method of thermal plant analysis*. Paragon Publishing, 2012.

[13] Lemmon E, Huber M, M. M. NIST Standard Reference Database 23, Reference Fluid Thermodynamic and Transport Properties (REFPROP), version 9.0, National Institute of Standards and Technology, R1234yf. fld file dated December 22 (2010). Technical report, NIST. URL `https://www.nist.gov/system/files/documents/srd/REFPROP8_manua3.htm`.

[14] Nondy, J. and Gogoi, T. Comparative performance analysis of four different combined power and cooling systems integrated with a topping gas turbine plant. *Energy Conversion and Management*, 223:113242, 2020.

[15] Palacios-Bereche, R., Gonzales, R., and Nebra, S. A. Exergy calculation of lithium bromide–water solution and its application in the exergetic evaluation of absorption refrigeration systems LiBr-H2O. *International Journal of Energy Research*, 36(2):166–181, 2012.

[16] Pátek, J. and Klomfar, J. A computationally effective formulation of the thermodynamic properties of LiBr-H2O solutions from 273 to 500 K over full composition range. *International Journal of Refrigeration*, 29(4):566–578, 2006.

[17] Safarian, S. and Aramoun, F. Energy and exergy assessments of modified Organic Rankine Cycles (ORCs). *Energy Reports*, 1:1–7, 2015.

[18] Salmi, W., Vanttola, J., Elg, M., Kuosa, M., and Lahdelma, R. Using waste heat of ship as energy source for an absorption refrigeration system. *Applied Thermal Engineering*, 115:501–516, 2017.

[19] Singh, O. K. and Kaushik, S. Variables influencing the exergy based performance of a steam power plant. *International journal of green energy*, 10(3): 257–284, 2013.

[20] Singh, O. K. and Kaushik, S. C. Reducing CO_2 emission and improving exergy based performance of natural gas fired combined cycle power plants by coupling Kalina cycle. *Energy*, 55:1002–1013, 2013.

[21] Srinivas, T. Study of a deaerator location in triple-pressure reheat combined power cycle. *Energy*, 34(9):1364–1371, 2009.

[22] Talbi, M. M. and Agnew, B. Exergy analysis: an absorption refrigerator using lithium bromide and water as the working fluids. *Applied Thermal Engineering*, 20(7):619–630, 2000.

[23] Tchanche, B. F., Papadakis, G., Lambrinos, G., and Frangoudakis, A. Fluid selection for a low-temperature solar organic Rankine cycle. *Applied Thermal Engineering*, 29(11-12):2468–2476, 2009.

[24] Yari, M. and Mahmoudi, S. M. A thermodynamic study of waste heat recovery from GT-MHR using organic Rankine cycles. *Heat and Mass Transfer/Waerme- und Stoffuebertragung*, 47(2):181–196, 2011.